Figure 1

Click here to access/download;Figure;Fig.1.png

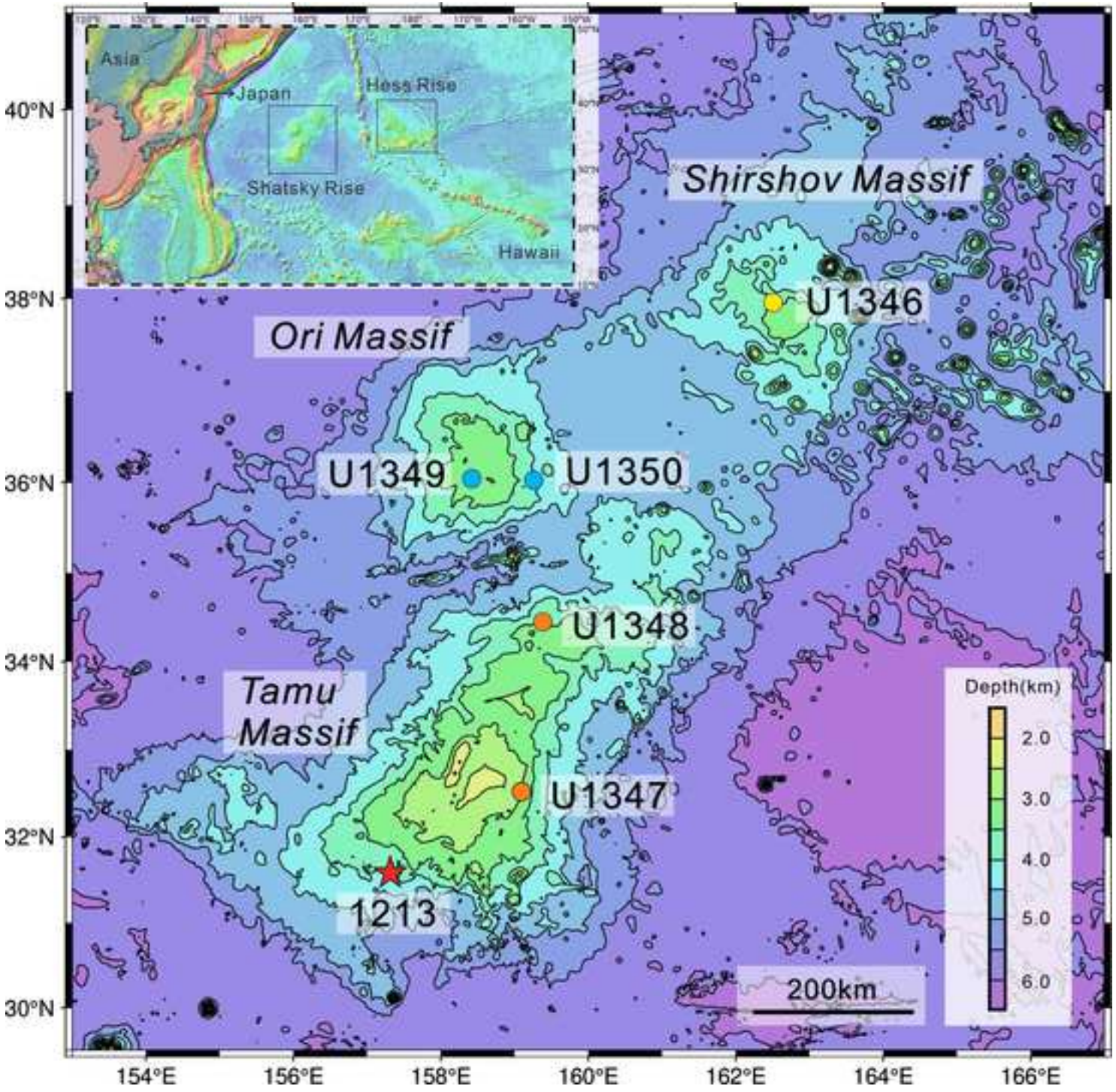

Figure 2

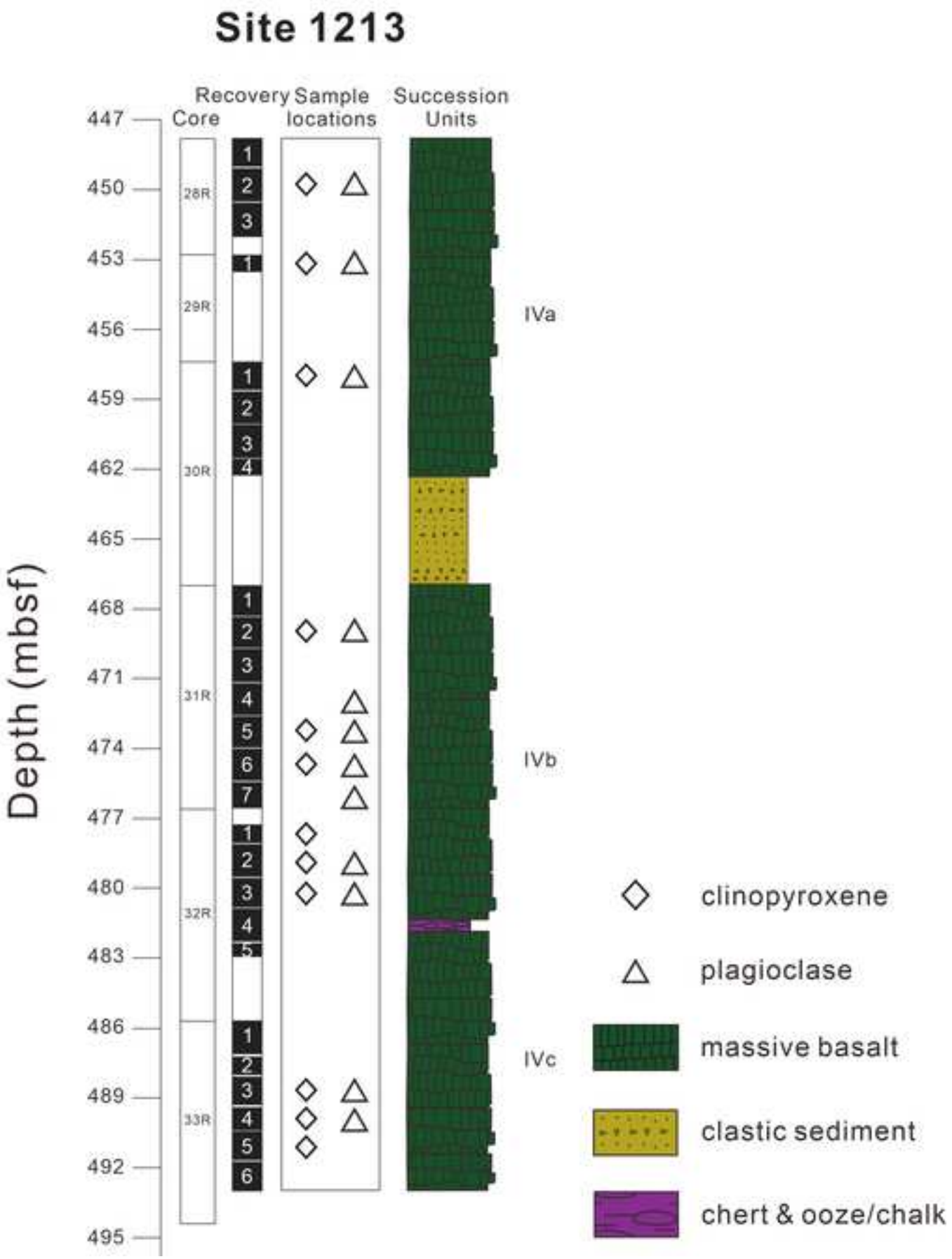

Figure 3

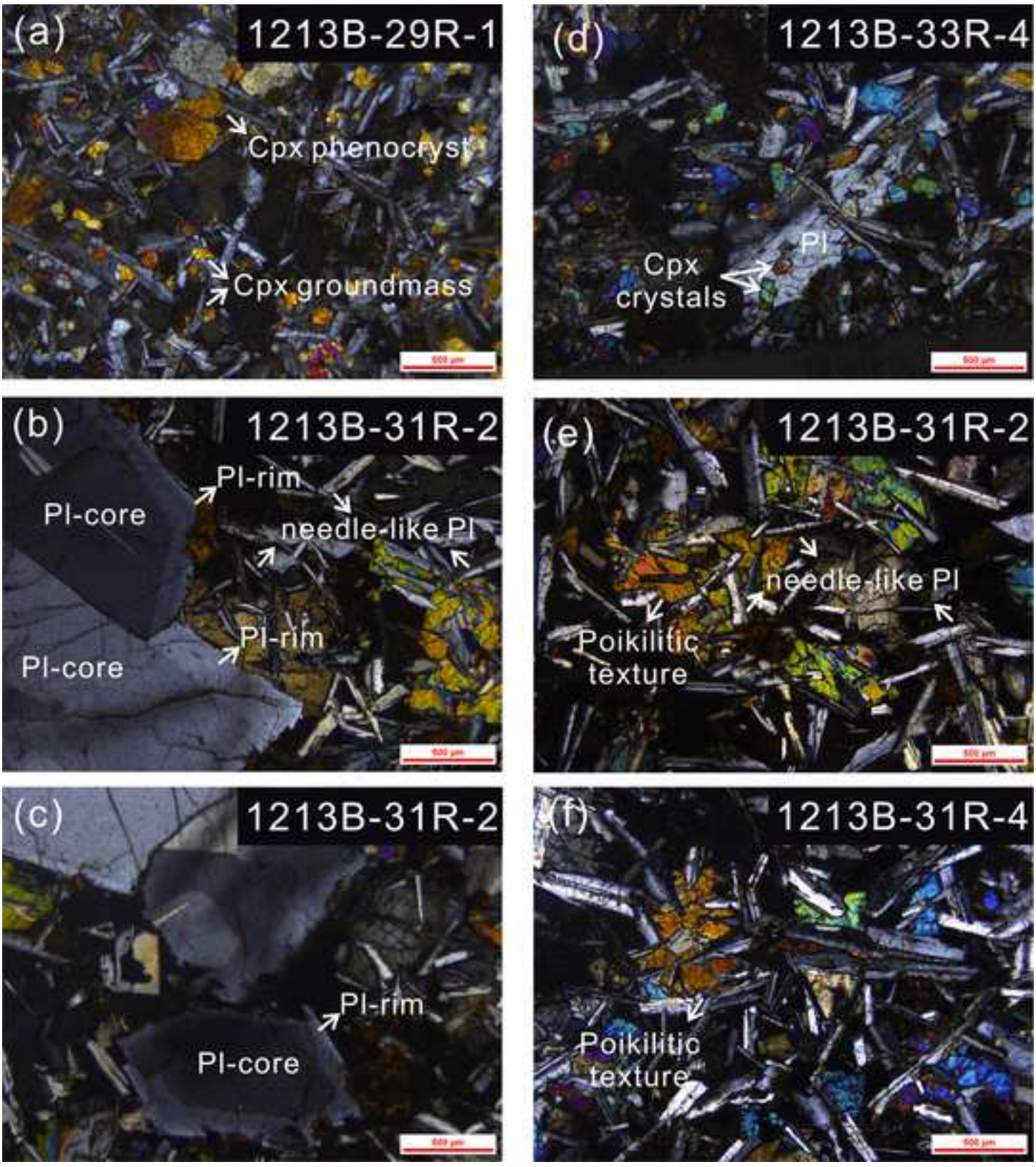

Figure 4

Click here to access/download;Figure;Fig.4.png

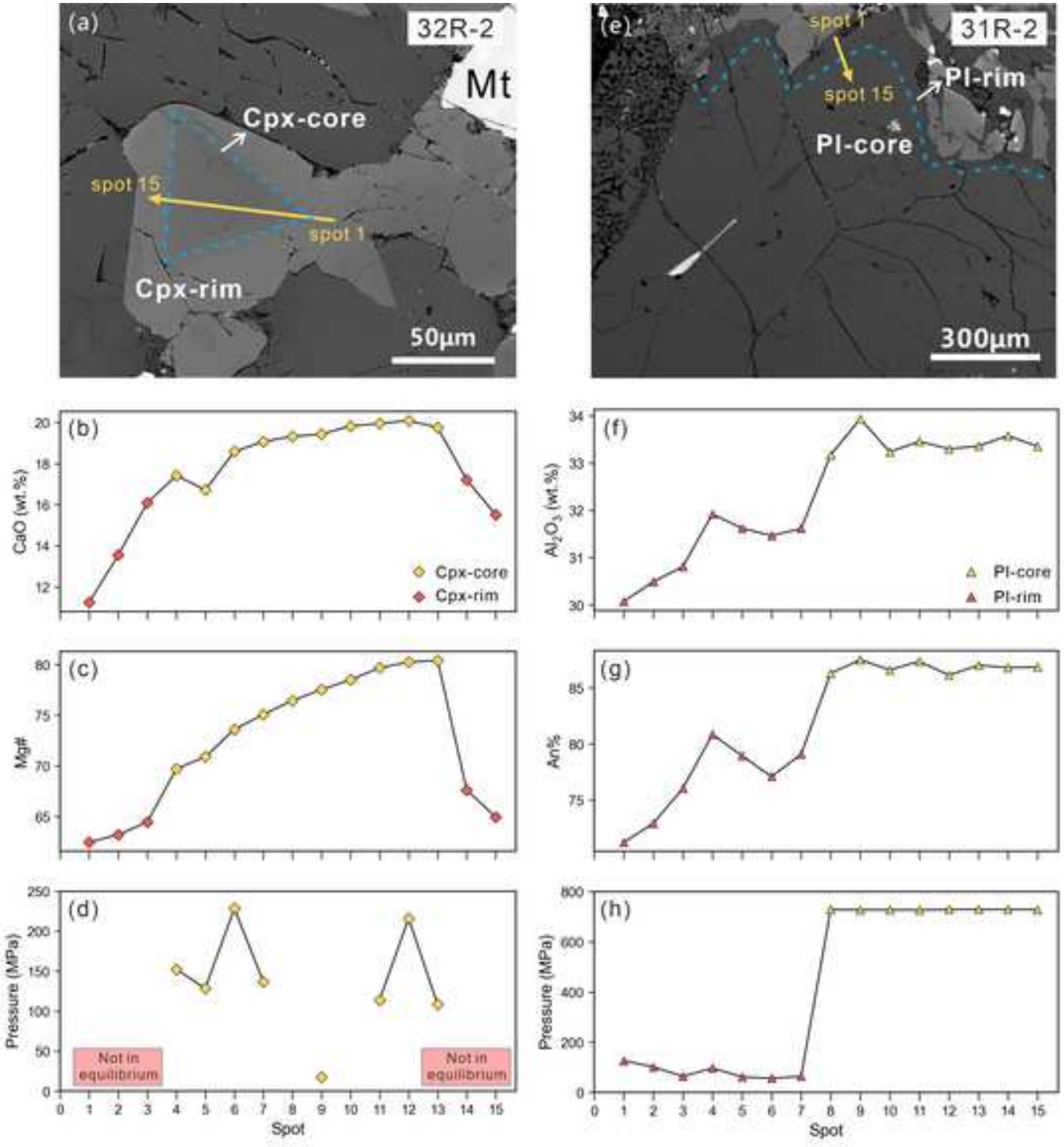

Figure 5

Click here to access/download;Figure;Fig.5.png

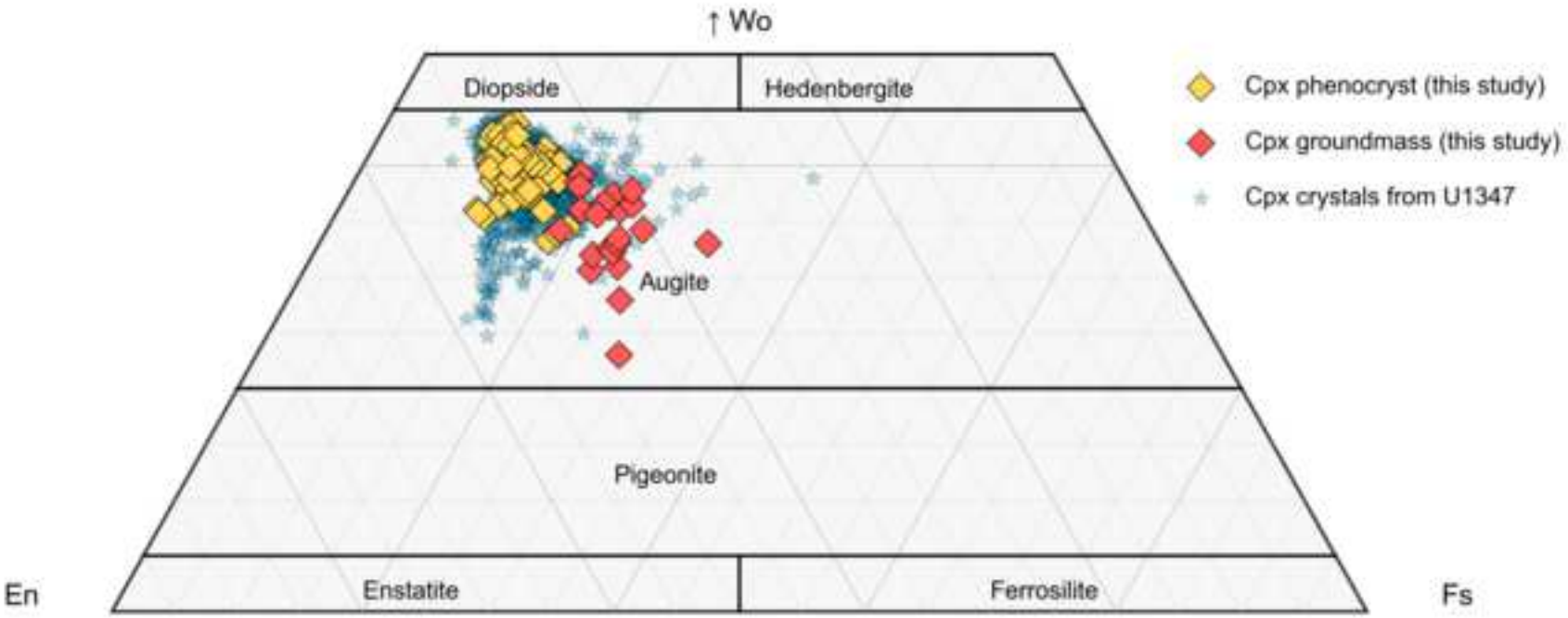

Figure 6

Click here to access/download;Figure;Fig.6.png

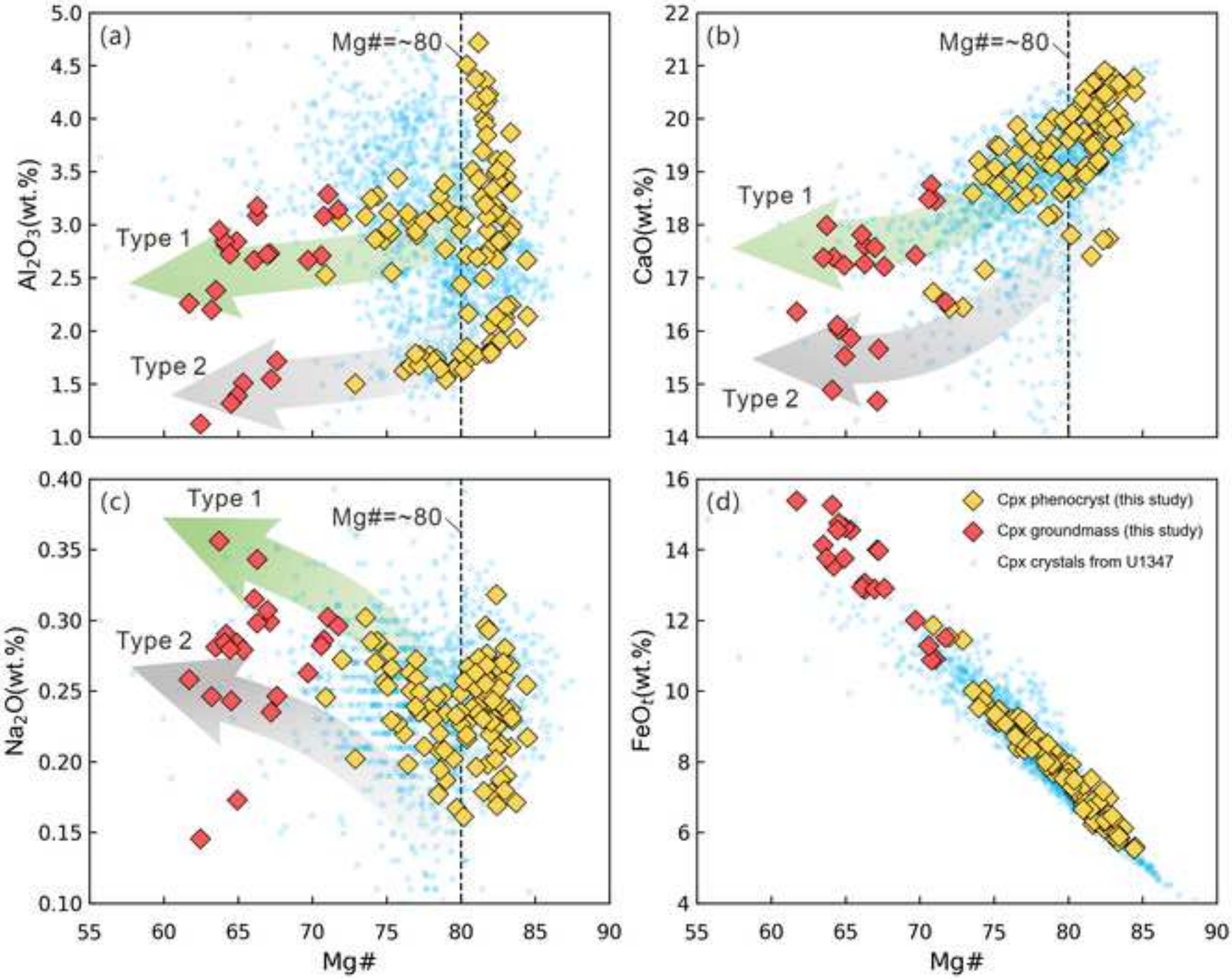

Figure 7

Click here to access/download;Figure;Fig.7.png

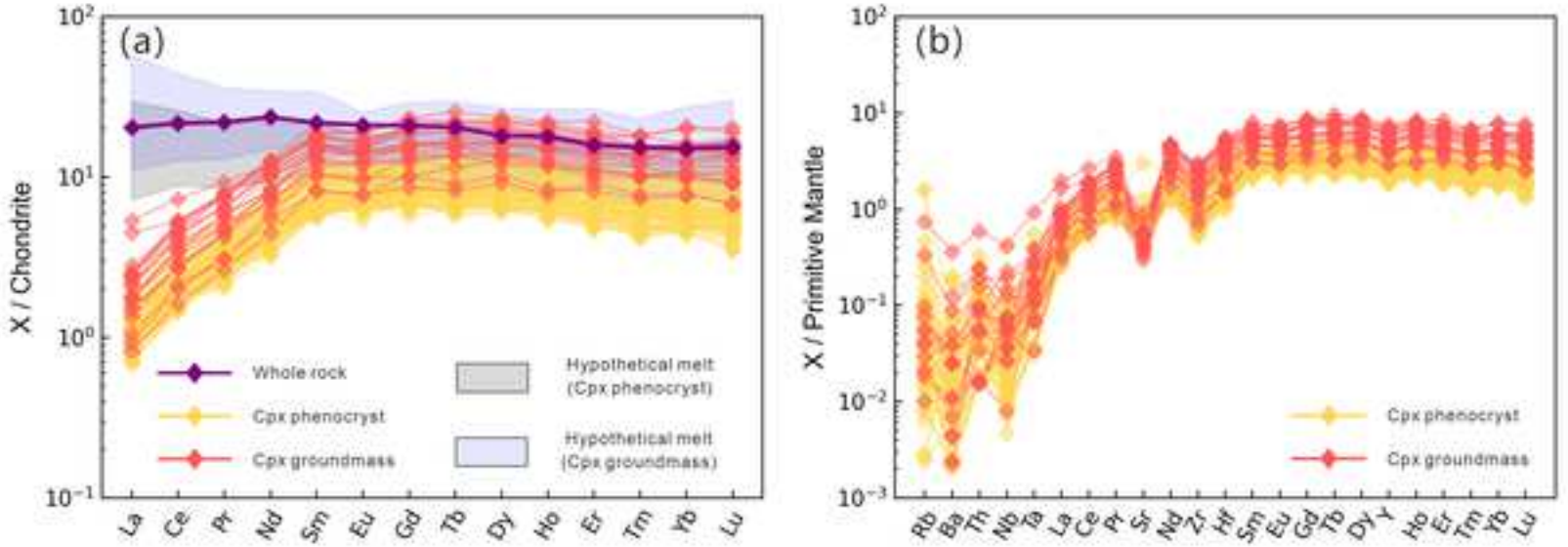

Figure 8

Click here to access/download;Figure;Fig.8.png

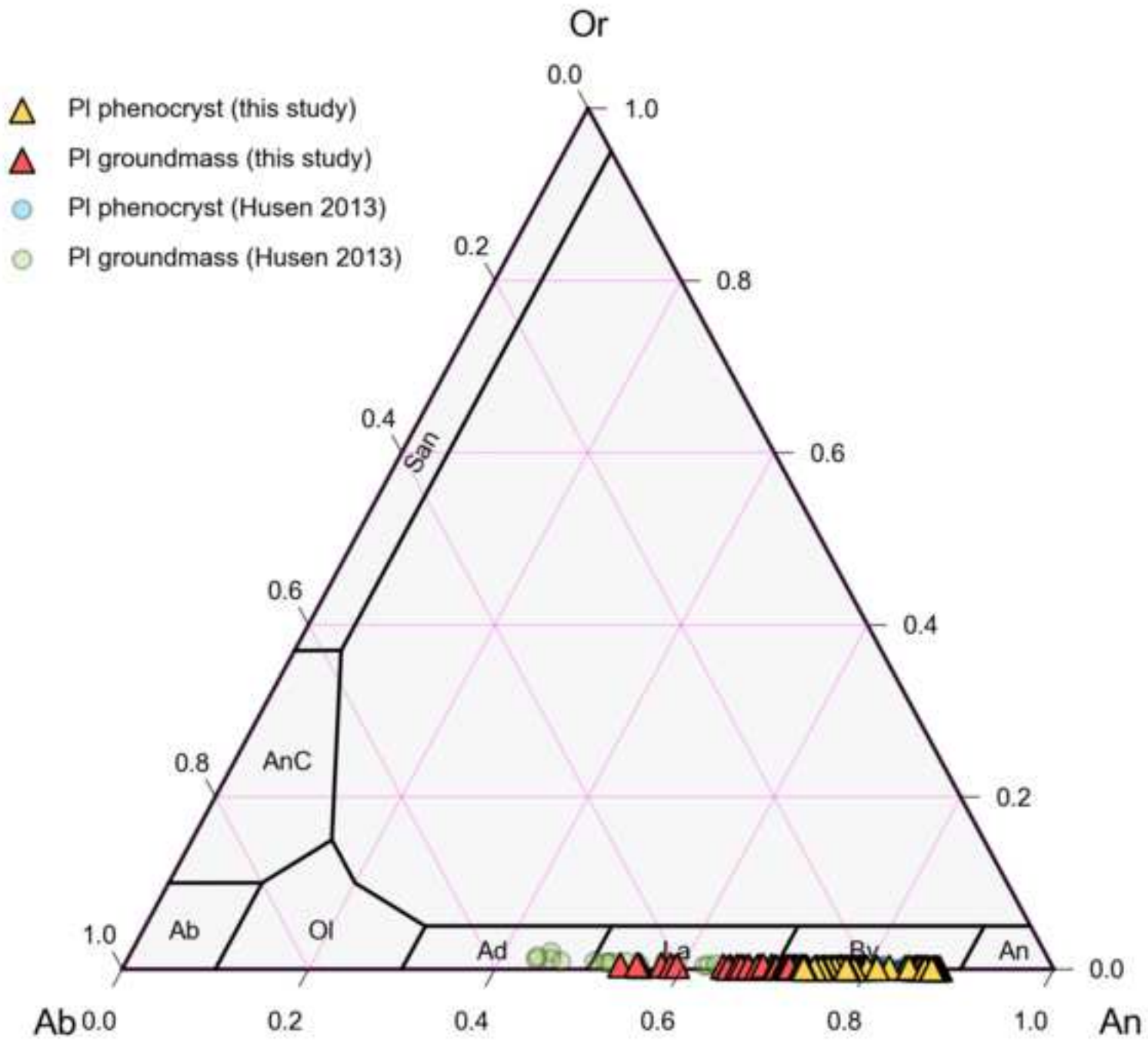

Figure 9

Click here to access/download;Figure;Fig.9.png

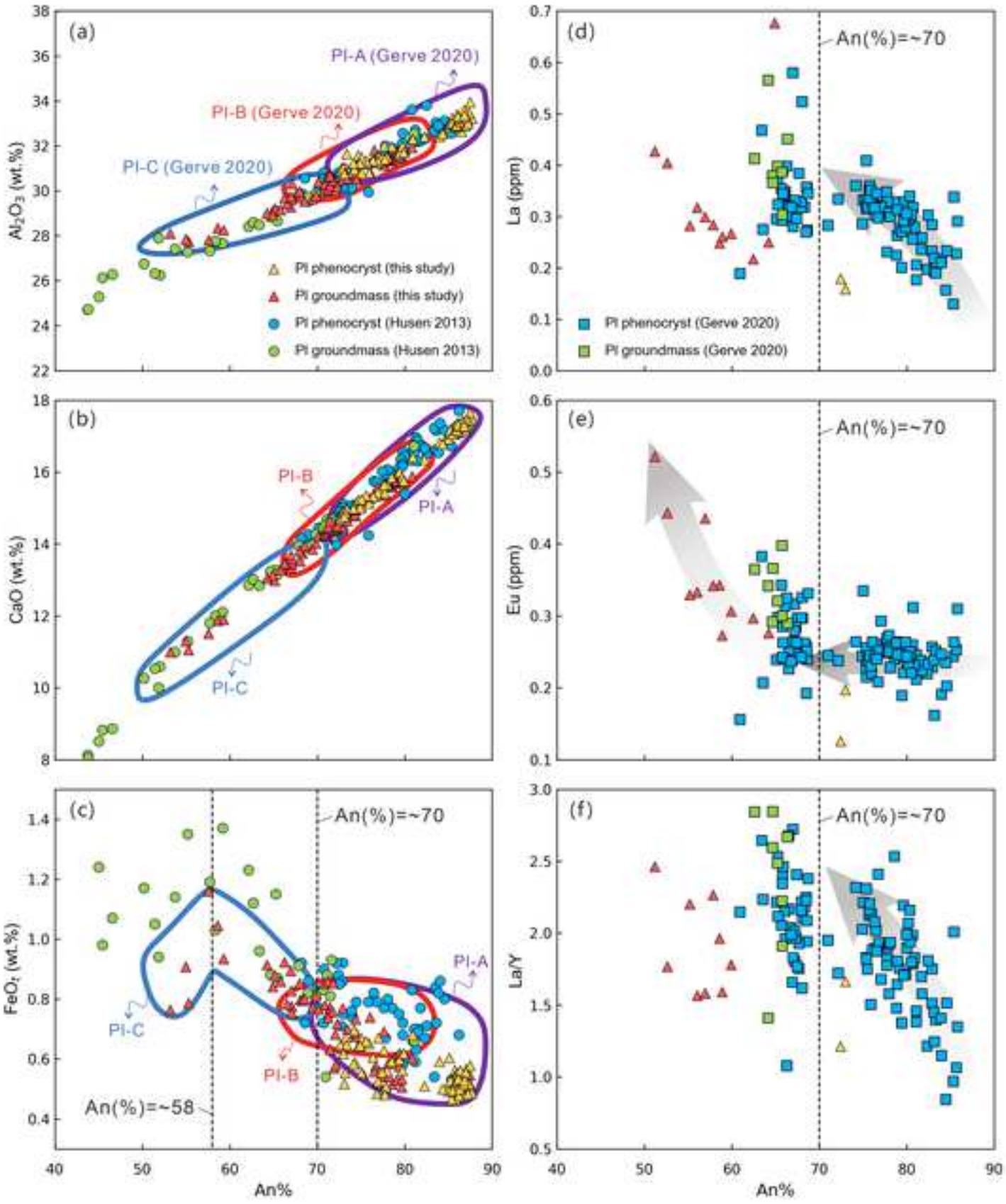

Figure 10

Click here to access/download;Figure;Fig.10.png

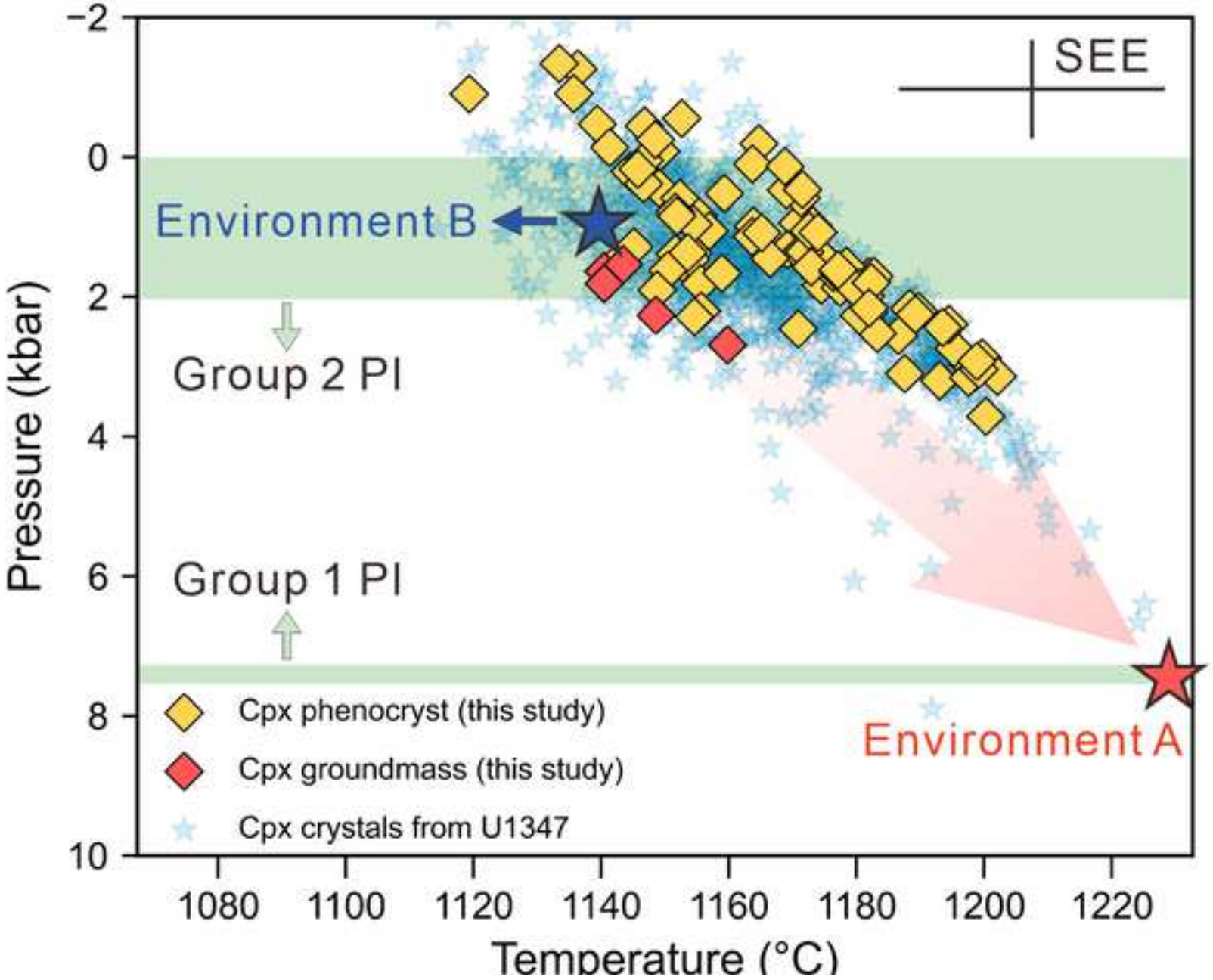

Figure 11

Click here to access/download;Figure;Fig.11.png

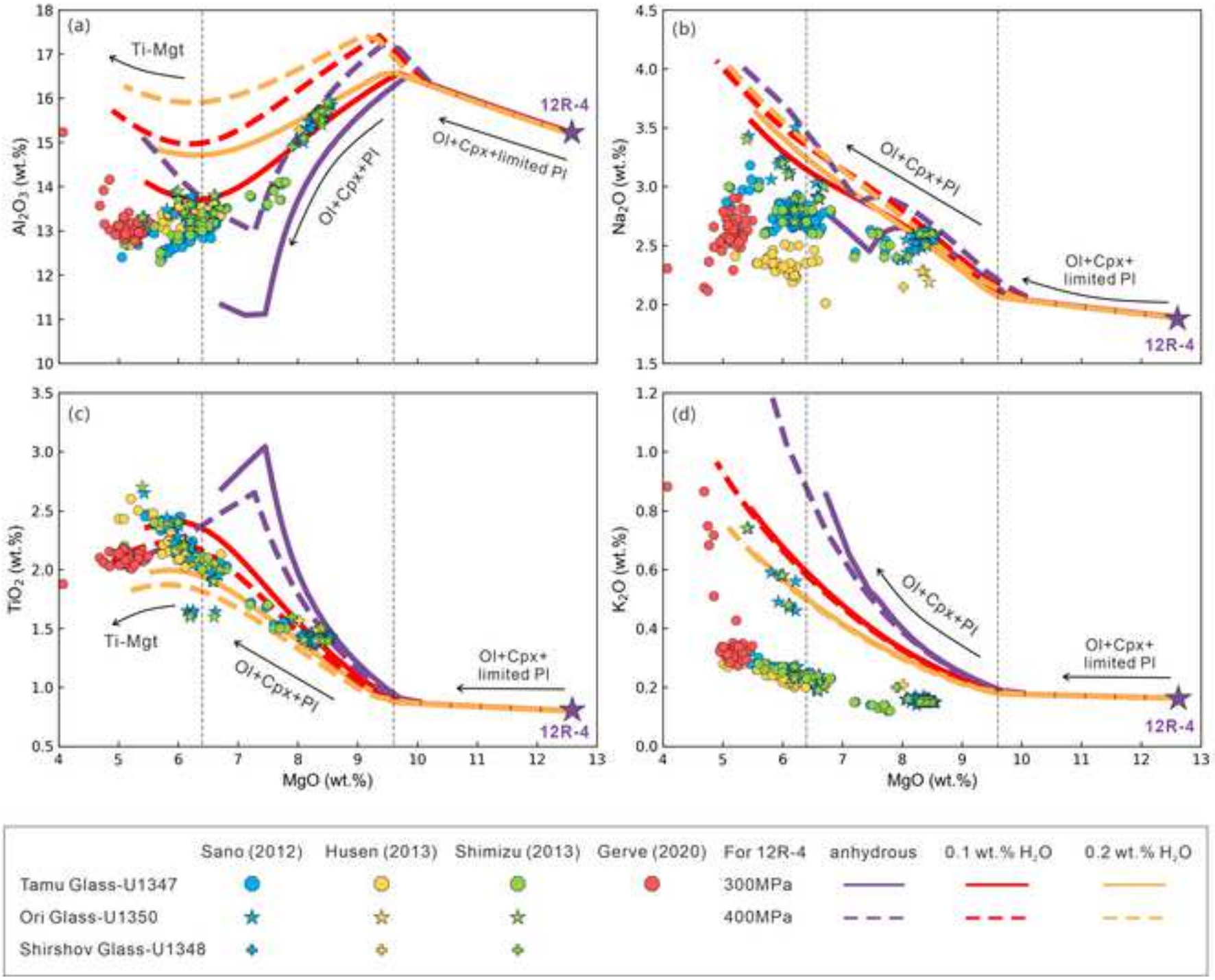

Figure 12

Click here to access/download;Figure;Fig.12.png

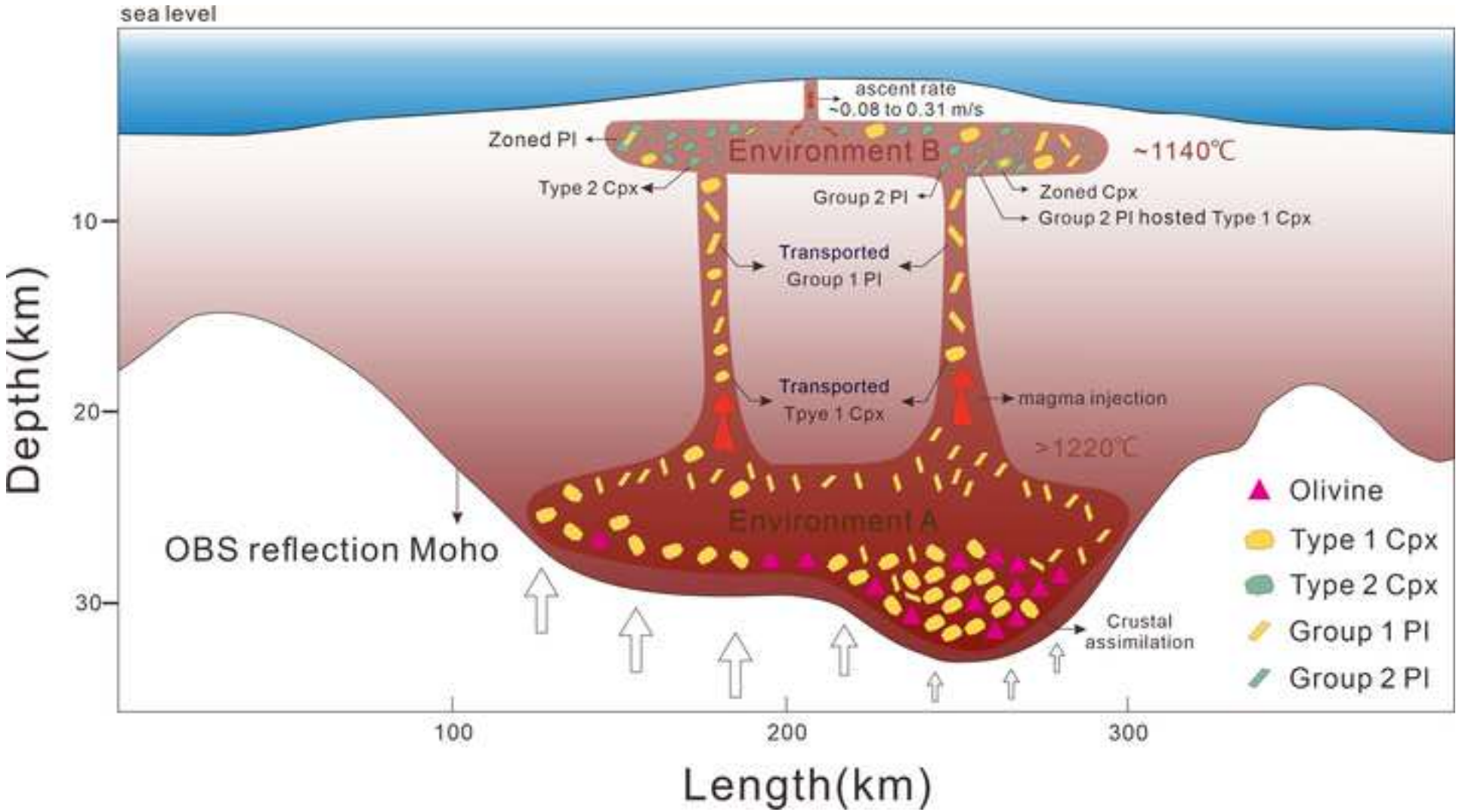

Figure 13

Click here to access/download;Figure;Fig.13.png

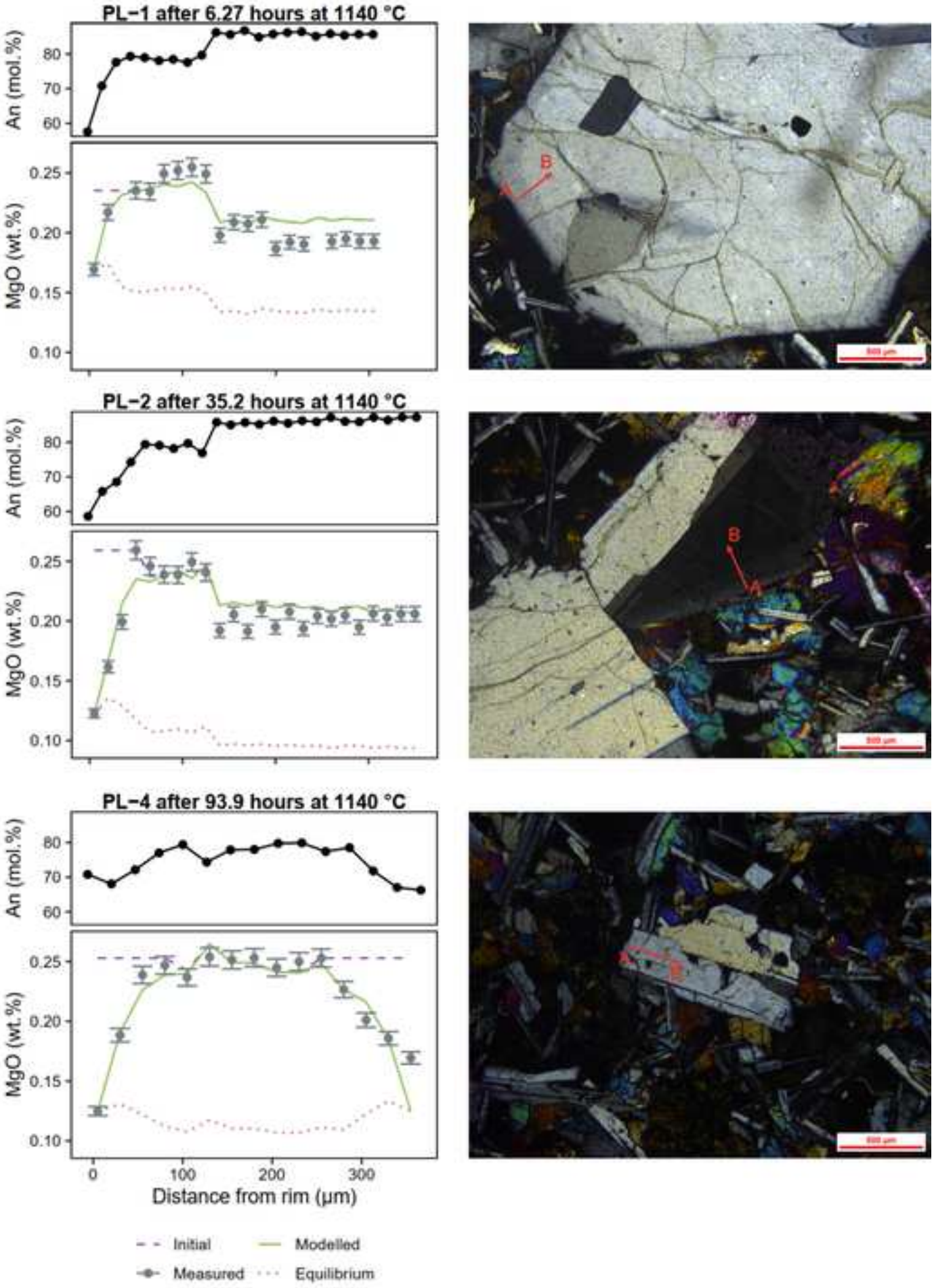

Figure 14

Click here to access/download;Figure;Fig.14.png

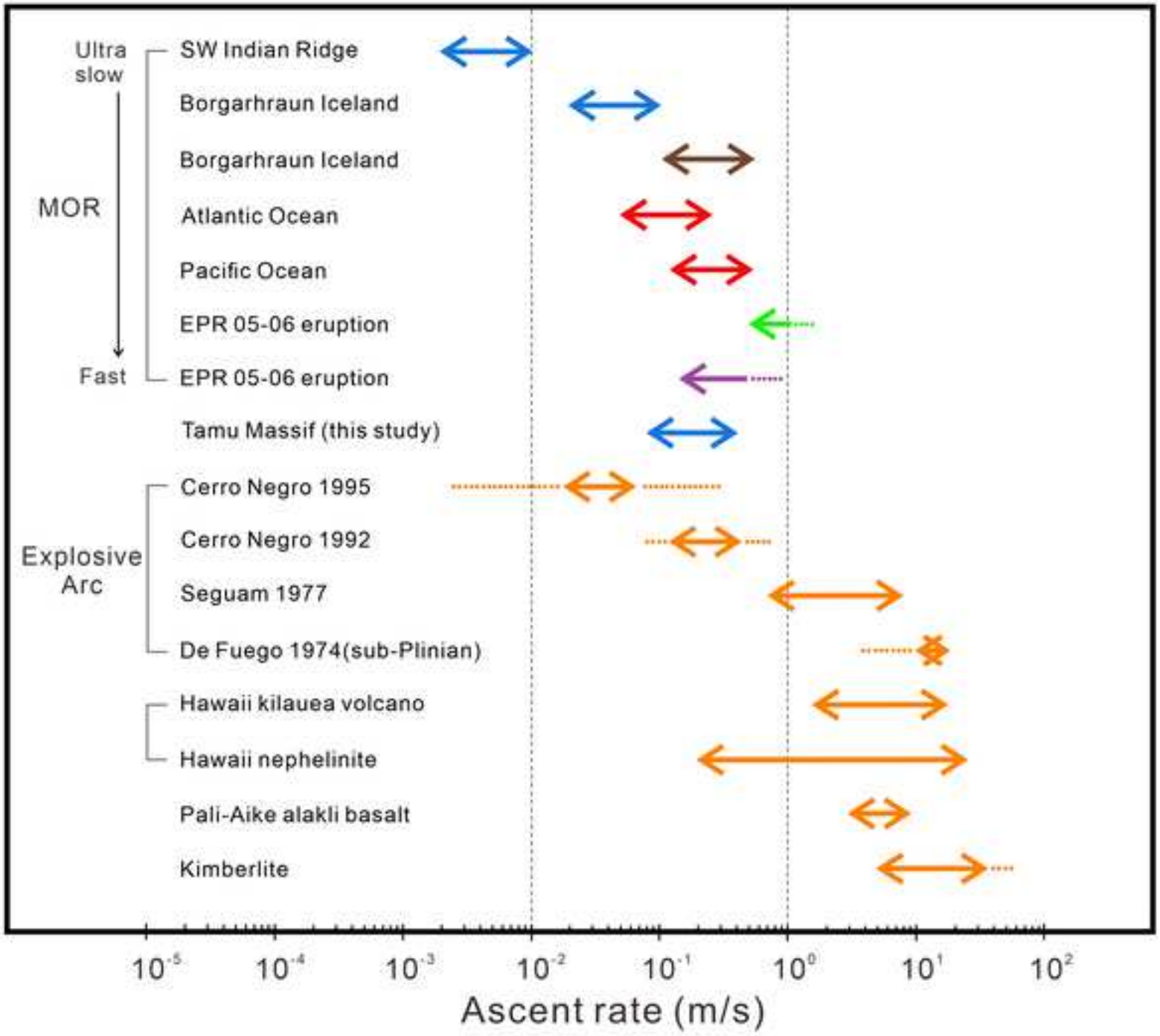

Table S1


Click here to access/download
Supplementary Material
Table S1.xlsx

Table S2


Click here to access/download
Supplementary Material
Table S2.xlsx

Table S3

Click here to access/download
Supplementary Material
Table S3.xlsx

Table S4

Click here to access/download
Supplementary Material
Table S4.xlsx

Table S5

Large Igneous Province magma plumbing system processes: insights from mineral chemistry and diffusion chronometry from the Shatsky Rise Oceanic Plateau, Northwest Pacific

Hengrui Zhu [a], Tao Wu [a, b, *], Shuangshuang Chen [c, *], Gareth N. Fabbro [d], Jianggu Lu [e], Ming Yang [b], Yidi Hong [a, b], Xueting Zhao [a], Haoyang Liu [a, b]

[a] *Ocean College, Zhejiang University, Zhoushan 316021, China*

[b] *Hainan Institute of Zhejiang University, Sanya 572025, China*

[c] *School of Earth Sciences and Engineering, Sun Yat-sen University, Guangzhou 510275, China*

[d] *School of Environmental Sciences, University of East Anglia, Norwich, United Kingdom*

[e] *Key Laboratory of Submarine Geosciences, Ministry of Natural Resources, Hangzhou 310012, China*

Corresponding author: E-mail addresses taowu@zju.edu.cn (T. Wu); chenshsh29@mail.sysu.edu.cn (S.S. Chen).

Abstract

Oceanic Large Igneous Provinces (LIPs) usually have abnormally thickened oceanic crusts and complex magma plumbing systems. Investigating the magma plumbing systems of LIPs is crucial for understanding the dynamic evolution of our Earth. The submarine Shatsky Rise oceanic plateau is the third largest oceanic plateau on Earth and reaches a maximum crustal thickness of 30 km at Tamu Massif, the oldest and largest volcanic edifice at the southwest of Shatsky Rise. Here, we present major-

trace elements of clinopyroxene (Cpx) and plagioclase (Pl) from Site 1213 of Ocean Drilling Program (ODP) Leg 198 at Tamu Massif. Based on the mineral chemistry and P-T calculations, we identified two types of Cpx and two groups of Pl. Type 1 Cpxs have higher Al_2O_3 (~3 wt.%), CaO (17~19 wt.%) and Na_2O (0.3~0.4 wt.%), and crystallized at greater depth and prior to the onset of plagioclase crystallization, whereas Type 2 Cpxs have relatively lower Al_2O_3 (~1.5 wt.%), CaO (14~16 wt.%) and Na_2O (0.2~0.3 wt.%), and crystallized at shallower depth and after significant plagioclases crystallization. The Pls can also be divided into two groups: Group 1 are the core of phenocrysts with high crystallization pressure (727 to 733 MPa) and An values (~85), whereas Group 2 are the rim of phenocrysts and groundmass with low crystallization pressure (< 204 MPa) and An values (< 75). Based on our new results, we propose a two-stage petrologic model to reveal the magmatic evolution at Tamu Massif. Stage 1 occurs at the Environment A, located within the lower crust (~ 25 km depth) with high crystal crystallization temperature (> 1220 ℃) and Stage 2 occurs at the Environment B, located within the shallow crust (~ 7 km depth) with low crystal crystallization temperature (~ 1140 ℃). Our MELTS modeling suggests the crystallization sequence is Ol-Cpx-Pl at Tamu Massif and Pl gradually replaced Cpx as the dominant fractionating phase at Environment B. The final transport time from Environment B to eruption on the seafloor is usually within a few days (6.27–93.9 hours), which is indistinguishable from the ascent rates of fast spreading ridge systems, but slower than those of volatile-rich magmas in explosive arc volcanos and kimberlites. This study improves our understanding of the formation and evolution of oceanic plateaus around

the world.

Key words: Shatsky Rise; MELTS modeling; Thermobarometer; Magma plumbing system; Diffusion chronometry

1. Introduction

As exceptional intraplate igneous events throughout the Earth's history, Large Igneous Provinces (LIPs) are characterized by huge volumes of magma intruded and erupted within a short period (Bryan and Ernst, 2008; Coffin and Eldholm, 1994). They have played a significant role in the ore deposit genesis and hydrocarbon resource formation (Bergman et al., 2021; Ernst and Jowitt, 2013; Nixon et al., 2022; Zhang et al., 2008), global environmental changes and mass extinction (Courtillot and Renne, 2003; Ernst et al., 2021; Jiang et al., 2023; Wignall, 2001), and dynamic evolution of the Earth (Black et al., 2021; Campbell, 2005; Coffin and Eldholm, 1992; Peace et al., 2020). Therefore, LIPs have attracted great attention from geologists, geophysicists and paleontologists. The earliest studied LIPs were in the continental areas known as the continental flood basalts (CFBs) (e.g., the Permian-Triassic Siberian Traps, Russia) and were widely thought to be formed by massive eruptions due to an upwelling mantle plume head (Carlson et al., 1981; Hooper, 1990; Richards et al., 1989). With the similar formation mechanism as the continental flood basalts, oceanic plateaus, submarine ridges, seamount groups and ocean basin flood basalts constitute the essential types of large igneous provinces in the ocean, representing an immense transfer of magma from

mantle to crust (Bryan and Ernst, 2008; Coffin and Eldholm, 1992; Coffin and Eldholm, 1994; Neal et al., 2019).

Recent research has shown that oceanic LIPs with abnormally thickened oceanic crusts usually have complex magma plumbing systems. For example, oceanic LIPs usually have multi-level storage and complex crystallization conditions, e.g., Hawaii (Tucker et al., 2019), Ontong Java (Kinman and Neal, 2006), Iceland (Neave and Putirka, 2017; Neave et al., 2013; Winpenny and Maclennan, 2011), and Azores (Métrich et al., 2014). Interestingly, basalts from oceanic LIPs are often geochemically similar to mid-ocean ridge basalts (MORB), based on the published major, trace elements and Sr-Nd-Pb-Hf isotopes of whole-rock and fresh glass samples (Chen et al., 2021; Heydolph et al., 2014; Sano et al., 2012). However, erupted liquids only provide a snapshot of the magmatic system's final state. In contrast, minerals that crystallize in the deep magma chamber provide valuable insights into the processes and conditions of transcrustal magma transport, storage and differentiation (Molendijk et al., 2022; Petrone et al., 2022; Ubide et al., 2021; van Gerve et al., 2020).

Clinopyroxene (Cpx) and plagioclase (Pl) phenocrysts are common in the oceanic plateau basalts, providing important tools to study the magmatic processes in the deep magma chamber (Hellevang and Pedersen, 2008; Holness et al., 2007; Lange et al., 2013; Li et al., 2020; Molendijk et al., 2022; Wei et al., 2022; Winpenny and Maclennan, 2011). For example, the compositional zoning of Cpx and Pl can record their crystallization and storage conditions at the scale of entire magma plumbing systems (Bennett et al., 2019; Petrone et al., 2022; Shcherbakov et al., 2011; Tapu et al., 2023;

89 van Gerve et al., 2020; Wei et al., 2022). During their long-crystallized history, the
90 composition of the Pl (such as trace element trends) can be affected by the co-
91 crystallization of Cpx. Furthermore, insights into the timescales of magmatic processes
92 can be derived by measuring the compositional profiles (Costa et al., 2020; Druitt et al.,
93 2012; Mutch et al., 2019). According to the complex plumbing systems of LIPs (Buchan
94 and Ernst, 2021; Ernst et al., 2019; Mittal et al., 2021), the combination of
95 clinopyroxene-based and plagioclase-based studies may shed new lights on the magma
96 plumbing systems in LIPs.

97 The submarine Shatsky Rise oceanic plateau, located ~1500 km east of Japan in
98 the northwest Pacific Ocean (Fig. 1), is the third largest oceanic plateau on Earth
99 covering an area of ~4.8×10^5 km^2 (Sager et al., 1999). From southwest to northeast,
100 Shatsky Rise comprises three main volcanic edifices: Tamu, Ori and Shirshov Massifs.
101 Tamu Massif is the oldest and largest edifice and reaches a maximum crustal thickness
102 of 30 km that is 2-4 times thicker than those of the world ocean abyssal basins (~ 7 km)
103 (Korenaga and Sager, 2012; Sager et al., 2013; White et al., 1992; Zhang et al., 2016),
104 implying extensive magma supply from the mantle. To explain this issue, hotspot–ridge
105 interaction was commonly assumed (Li et al., 2016; Zhang and Chen, 2017; Zhang et
106 al., 2023). However, details of magmatic evolution and timescales of magmatic
107 processes still remain unclear (Huang et al., 2018; Sager et al., 2016; van Gerve et al.,
108 2020).

109 In this study, we focused on Site 1213 by Ocean Drilling Program (ODP) Leg 198,
110 which is located at Tamu Massif, the southwest end of the Shatsky Rise. To investigate

111 the magma plumbing system and track timescales of magmatic processes here, we
112 present an integrated study of petrography, mineral chemistry, MELTS modeling and
113 diffusion chronometry. We aim to constrain Cpx and Pl crystallization conditions, as
114 well as magma residence and ascent timescales at Tamu Massif to understand the
115 processes and conditions of magma transport, storage and differentiation in oceanic
116 plateaus.
117
118 **2. Geological setting and samples**
119 Volcanic eruptions of Shatsky Rise oceanic plateau started 147 Ma (polarity chron
120 M20) at Tamu Massif and continued to 139 Ma (M13) with successive emplacement of
121 the Ori and Shirshov Massifs (Nakanishi et al., 1999). Unlike mid-Cretaceous plateaus
122 (e.g., Ontong Java–Manihiki–Hikurangi and Kerguelen), Shatsky Rise was formed at
123 the Jurassic-Cretaceous boundary, when magnetic reversals were occurring (Nakanishi
124 et al., 1999; Nakanishi et al., 2015; Sager et al., 1988). The elongated shape and
125 magnetic lineations of Shatsky Rise suggest that melting was controlled by spreading-
126 ridge tectonics (Sager et al., 2019). The oldest and largest Tamu Massif (~144.6 Ma,
127 2.5×10^6 km^3) was followed by younger and smaller Ori (~138 Ma, 0.7×10^6 km^3) and
128 Shirshov Massifs (~137Ma, 0.5×10^6 km^3) (Mahoney et al., 2005; Nakanishi et al.,
129 2015). This temporal succession is in line with a plume model for the generation of
130 Shatsky Rise, in which Tamu Massif marks the arrival of the plume head and the
131 decreased magma production in the younger massifs represents the transition to the
132 plume tail (Sager et al., 1999; van Gerve et al., 2020; Zhang et al., 2023).

Ocean Drilling Program Leg 198, which sailed in 2001, was the first expedition to penetrate into igneous basement of Shatsky Rise at Site 1213 on the southwest flank of Tamu Massif (Fig. 1). Drilling extracted 46.6 m of basaltic rock at a high recovery of 72.3% (Bralower et al., 2002) and our samples are from the igneous basement unit (IV) of Site 1213 (Fig. 2). In thin sections, Tamu Massif volcanic samples at Site 1213 are featured by relatively high crystallinity, exhibiting a porphyritic texture with phenocrysts of mainly clinopyroxene (30%-35%) and plagioclase (55%-60%) (Fig. 3). Clinopyroxene phenocrysts range from small euhedral crystals to somewhat larger grains (0.5–1 mm) and clinopyroxene in this study shows no obvious sector zoning (Fig. 3a). Lots of fine clinopyroxene groundmass (< 0.2 mm) show anhedral shapes filling the gap of the plagioclases. Plagioclase phenocrysts occur as intact needle-like (0.5–1 mm) and relatively large (>3 mm) crystals (Figs. 3b and 3c). Some of the large grains have external overgrowths with rims of normal zoning and plagioclase groundmass are prismatic and generally 0.5 mm or shorter in length. The thin sections show typical poikilitic texture with small clinopyroxene crystals enclosed within large plagioclase crystals (Fig. 3d) and needle-like plagioclase enclosed within clinopyroxene phenocrysts (Figs. 3e and 3f). Skeletal and dendritic titanomagnetite (< 2 %) also exists in some samples. Note that we do not observe olivine in any of the thin sections at Site 1213 because they are completely replaced by dull greenish brown clays.

3. Analytical methods

After careful examination under a microscope, twenty plagioclase crystals from

twelve different core sections and thirty clinopyroxene crystals from twelve different core sections were selected for major and trace element analyses at Site 1213 (Fig. 2). Table S1 and S2 list the detailed information of the investigated samples.

3.1 Mineral major element chemistry: EPMA

Chemical compositions of plagioclase and clinopyroxene phenocrysts were measured on polished thin sections by a four-spectrometer Jeol JXA 8100 electron probe microanalyzer (EPMA) in the Key Laboratory of Submarine Geoscience, State Oceanic Administration, Second Institute of Oceanography (Hangzhou, China). Back-scattered electron images were utilized to check the homogeneity of the phenocrysts and the crystal zoning. We used an accelerating potential of 15 kV, a beam current of 20 nA and a spot size of 5 um in most analyses, whereas small minerals were analyzed using a 1~3 um spot. Jadeite (Si and Na), olivine (Mg), almandine garnet (Fe and Al), diopside (Ca), sanidine (K), rutile (Ti), and rhodonite (Mn) were used for calibration standards. Element peaks and backgrounds were measured for all elements with counting times of 10 s and 5 s, respectively (except for Fe, Mn, that were 30 s and 15 s, respectively). Each sample was analyzed 10 times in different locations, with the mean compositions being reported in Table S1. The precision (1σ) is <3% for Si, Al, Fe, Mg, and Ca, 15% for Ti, Na, and K.

3.2 Mineral trace element chemistry: LA-ICP-MS

Trace element analyses of clinopyroxenes were conducted at the laser ablation-induced coupled plasma-mass spectrometry (LA-ICP-MS) laboratory in the School of Earth Science, Zhejiang University, China. The analytical instrument includes an iCAP-

177 RQ single-collector quadrupole ICP-MS (Thermo Fisher Scientific, Waltham, USA)
178 coupled to an Analyte G2 ArF excimer laser ablation (LA) system equipped with HelEx
179 2 volume sample chamber (Teledyne Cetac Technologies, Omaha, USA). The spot size
180 and frequency of the laser were set to 60 μm and 5 Hz respectively, and we did not
181 analyze the mineral zones. The fluence of the laser analyse was 18 J/cm^2. Each analysis
182 incorporated a background acquisition of approximately 20–30 s followed by 50 s of
183 data acquisition from the sample. Two geochemically distinct reference glasses (BCR-
184 2G, BHVO-2G) were used to cover the possible geochemical spectrum. Every 8 sample
185 analyses were followed by two analyses of NIST SRM 610 to correct the time-
186 dependent drift of sensitivity and mass discrimination. We employed a multi-external-
187 standard without internal-standard approach, processing our data using the
188 ICPMSDataCal software (Liu et al., 2008). The software was used to perform off-line
189 selection and integration of background and analytic signals, as well as time-drift
190 correction and quantitative calibration for trace element analysis. Relative standard
191 deviations (% RSD) of LA-ICP-MS analyses are less than 10% for all trace elements.
192 The trace elements of clinopyroxenes and plagioclases are presented in Table S2. The
193 trace element values of standard samples during the mineral analyzing process are also
194 presented in Table S2.
195
196 **4. Results**
197 4.1 Zoning texture of clinopyroxene and plagioclase
198 Inferred from backscatter electron images and compositional characteristics, only

a few clinopyroxenes at Site 1213 display normal zoning. However, the results of electron probe analysis demonstrate that their geochemical compositions vary from the core to the rim. The clinopyroxene phenocryst shows the highest CaO (up to 20.10 wt.%), Mg# (> 80) contents in the core, and the values of CaO and Mg# gradually decrease from the core to the rim (CaO = 11.25 wt.%; Mg# = 62) (Fig. 4). Clinopyroxenes show no obvious sector zoning. Numerous plagioclase phenocrysts are optically zoned (Figs. 3 and 4). As shown in Figs.4f and 4g, the Ca-rich plagioclase phenocryst has the highest Al_2O_3 (up to 33.94 wt.%), An (up to 87.5) contents in the core, but the lowest Al_2O_3 (~30.08 wt.%), An (~71) in the rim. The details about the normal zoning texture of clinopyroxene and plagioclase can be found in Table S1.

4.2 Major and trace element compositions of clinopyroxene

Clinopyroxene is one of the major phases in our samples. The major- and trace-element compositions of clinopyroxene can be used to calculate crystal chemistry, crystallization temperature, pressure, and the composition of equilibrium melts (Neave and Putirka, 2017; Putirka, 2008; Sun and Liang, 2012). Based on the classification of pyroxene proposed by Morimoto (1988), most of pyroxenes at Site 1213 are augites with compositions of $Wo_{23\text{-}44}En_{36\text{-}53}Fs_{9\text{-}31}$ $\left(Wo = 100 \times Ca/(Mg + Fe + Ca); En = 100 \times Mg/(Mg + Fe + Ca); Fs = 100 \times Fe/(Mg + Fe + Ca)\right)$ (Fig. 5). Clinopyroxene phenocrysts range in composition from $Wo_{33\text{-}44}En_{44\text{-}53}Fs_{9\text{-}19}$, whereas Cpx groundmass crystals are more ferrosilitic: $Wo_{23\text{-}40}En_{36\text{-}49}Fs_{17\text{-}31}$. Clinopyroxene compositions in this study are similar to Cpx crystals from Site U1347(Husen et al.,

2013; van Gerve et al., 2020), which was another core at Tamu Massif and drilled during Expedition 324 of the Integrated Ocean Drilling Program (Sager et al., 2010).

Clinopyroxene phenocrysts have higher Al_2O_3 (1.50-4.72 wt.%), CaO (16.43-20.90 wt.%), and Mg# values ($Mg\# = 100 \times Mg/(Mg + Fe)$, where Mg and Fe represent molar proportions and the iron in Cpx is Fe^{2+}) (70.9–84.5) and lower Na_2O (0.16–0.32 wt.%), FeO_t (5.53–11.85 wt.%), and TiO_2 (0.35–0.87 wt.%) contents than those of Cpx in groundmass (Al_2O_3 = 1.12-3.29 wt.%; CaO = 11.25-18.75 wt.%; Mg# = 53.7–71.8; Na_2O = 0.15–0.36 wt.%; FeO_t = 10.87–18.56 wt.%; TiO_2 = 0.60-1.23 wt.%; Table S1). Clinopyroxenes at Site 1213 display positive correlations between CaO, Cr, Ni and Mg# values, weak positive correlation between Al_2O_3 and Mg# values with lots of scatter compared to the other diagrams, negative correlations between Na_2O, FeO_t, TiO_2, Yb, Y and Mg#, and no correlation between Sr and Mg# (Figs. 6 and S1). Note that there is no straightforward negative correlation for Na_2O when Mg# > 80, because the variation in melt compositions which the Cpx crystallized from could result in Na_2O heterogeneity in Cpx. Clinopyroxene phenocrysts have much higher Cr (28.8-6911.0 ppm), Ni (115.3-199.3 ppm), and much lower Yb (0.74–1.78 ppm) contents than those of Cpx in groundmass (Cr = 1.2-119.5 ppm; Ni = 25.6-126.7 ppm; Yb = 1.29–3.48 ppm).

All Site 1213 clinopyroxenes generally exhibit the depletion of light REEs (LREEs; La_N = 0.69–5.35 ppm) and the enrichment of heavy REE (HREEs; Yb_N = 4.37–20.49 ppm; Table S2) relative to chondrite. In the chondrite-normalized rare earth element (REE) plots, all Cpx crystals display parallel and left-inclined REE patterns

and almost identical trace element distribution patterns (Fig. 7a). Cpx in groundmass have higher REEs (La_N = 0.83–5.35 ppm; Yb_N = 6.67–20.49 ppm; ∑REEs = 13.30-35.91 ppm) than Cpx phenocrysts (La_N = 0.69–2.63 ppm; Yb_N = 4.37–10.50 ppm; ∑REEs = 9.54-30.49ppm), whereas there is no significant difference in La_N/Yb_N and Sm_N/Yb_N ratios between Cpx phenocrysts and groundmass (Fig. S1f). In the primitive mantle-normalized multielement spectra, Site 1213 clinopyroxenes exhibit significant Th enrichment and Ba, Nb, Sr, Zr and Y depletion (Fig. 7b). It should be noted that Cpx in groundmass have subtle depletion in Sr and Eu than Cpx phenocrysts (Figs. S1c and 7). Following the model by Sun and Liang (2012) and assuming the temperature of 1200°C and 1140°C for Cpx phenocrysts and groundmass, we calculate the partition coefficients ($K_D(Fe\text{-}Mg)^{Cpx\text{-}melt}$) between coexisting Cpx and melt and then model the REE patterns of the parental melts in equilibrium with Cpx. The grey and purple shaded areas in Fig. 7a show REE patterns for hypothetical melts in equilibrium with Cpx phenocrysts and groundmass respectively, which are similar to those of the host-rocks (the purple line in Fig. 7a).

4.3 Major and trace element compositions of plagioclase

Numerous plagioclase phenocrysts are observed in volcanic samples at Site 1213. Most of feldspar minerals at Site 1213 are Ca-rich plagioclases (labradorite, bytownite) with variable compositions of $Ab_{12–46}An_{53–88}Or_{0-1}$ ($Ab = 100 \times Na/(K + Na + Ca)$; $An = 100 \times Ca/(K + Na + Ca)$; $Or = 100 \times K/(K + Na + Ca)$) (Table S1; Fig. 8). At Site U1347, Husen et al. (2013) found some of plagioclase groundmass are andesine (An < 50), which are not found in this study. The results show that the

compositions of the plagioclase phenocrysts range in composition from 72 to 88 mol% An, whereas the rims of plagioclase and groundmass crystals are more albitic: 53–81 mol % An.

The plagioclases at Site 1213 display positive correlations between Al_2O_3, CaO and An values, and negative correlations between Na_2O, K_2O, FeO_t, TiO_2, La, Eu and An values (Fig. 9). It is important to note that FeO_t and Eu contents have not been obviously increased with the decrease of An values (An > 70), nevertheless, they have a sudden increase when An < 70 (Figs. 9c and 9e). When An < 58, the slightly decreasing FeOt and TiO_2 contents with decreasing An values likely indicate crystallization of titanomagnetite (Fig. 9c). Due to clinopyroxene preferentially incorporating Y over La (Vannucci et al., 1998) whereas plagioclase does not (Aigner-Torres et al., 2007), the obvious increasing La/Y ratios with decreasing An values likely indicates crystallization of clinopyroxene when An > 70 (Fig. 9f). The La and La/Y ratios do not correlate with An values when An < 70 (Figs. 9d and 9f). Some plagioclase trace element compositions in Fig. 9 are from literature data (Husen et al., 2013; van Gerve et al., 2020).

5. Discussion

5.1 Mineral-melt equilibrium and P-T constraints

Previous studies have suggested that volcanoes situated on thick oceanic crust usually have at least two vertically separated storage regions and multi-level differentiation (Baxter et al., 2023; Caracciolo et al., 2023; Husen et al., 2013; Neave

287 and Putirka, 2017; van Gerve et al., 2020). For example, deep magma reservoirs are
288 presumably located near the Moho and solidified shallow magma reservoirs are thought
289 to form gabbro in the lower oceanic crust (Sager et al., 2016). Therefore, it is important
290 to estimate the depth of magma reservoirs. Previous studies suggested that
291 clinopyroxene and plagioclase crystals that are transported through the crust and stored
292 at different depths would develop textural zonation and record the magma condition
293 (Ginibre et al., 2007; Petrone et al., 2022; Streck, 2008; Tapu et al., 2022). Thus, the
294 depth of magma reservoirs can be estimated through calculating the crystallization
295 pressure of mineral crystals by using thermobarometers (Neave and Putirka, 2017;
296 Putirka, 2008). However, to use Cpx-melt and Pl-melt thermobarometer, the
297 composition of the melt must be in equilibrium with the crystalized Cpx and Pl. In this
298 study, pressures and temperatures from Cpx-melt and Pl-melt equilibria were calculated
299 by using the open-source Python3 package Thermobar v. 1.0.41 (Wieser et al., 2022).
300 Details of the methods are shown in the Supplementary Text S1 and S2. Equilibrium
301 was assessed between all mineral-liquid pairs by using reference values from Putirka
302 (2008) with liquids composition from the literature (Husen et al., 2013; Sano et al.,
303 2012; Shimizu et al., 2013; van Gerve et al., 2020). In this study, most of the Cpx
304 phenocrysts are unzoned crystals. For zoned Cpx, no liquids could be found in
305 equilibrium with the rim composition (Table S4).

306 Here, we estimated the pre-eruptive temperatures and pressures by using
307 thermobarometers from Cpx-melt thermometer presented in eq. 33 of Putirka (2008)
308 and Cpx-melt barometer presented in Neave and Putirka (2017). The calculated

crystallization temperature and pressure of Cpx phenocrysts are from 1142.3 ℃ to 1202.1 ℃ and less than 371 MPa (N=92), whereas those of Cpx groundmass are from 1140.4 ℃ to 1159.8 ℃, and from 154 to 269 MPa (N=5), respectively. According to the calibration errors of Cpx-melt thermometer and barometer (SEE = ± 42°C and SEE = ± 140 MPa, respectively) (Neave and Putirka, 2017; Putirka, 2008), P-T conditions are similar between Cpx phenocrysts and groundmass (Fig. 10). However, the wide range of crystallized pressure of Cpx phenocrysts may indicate that they have may crystallized during ascent of the host melts. Site U1347 is on the eastern flank of Tamu Massif and located northeast to Site 1213 (Koppers et al., 2010). We collect the literature data (Table S3) (Husen et al., 2013; van Gerve et al., 2020) and use the same thermometer and barometer (Putirka, 2008) to calculate P-T conditions (see Supplementary Text S1 for details) for comparison. The calculation results (1114.5 ℃ to 1225.1 ℃ and less than 790 MPa; N=1081) match well with our results from Site 1213 (Fig. 10).

According to the REE-in-plagioclase–clinopyroxene geothermometer (see Supplementary Text S2 for details; Sun and Liang, 2017), REE equilibration temperatures of plagioclase in this study range from 1230 ℃ to 1130 ℃. A total of 135 plagioclases were in equilibrium with melt composition in this study and were used to calculate crystallization pressure by the eq. 25a of Putirka (2008) (see Supplementary Text S2 for details). The results can be divided into two groups: Group 1 Pls have crystallization pressure from 727 to 733 MPa (N=38), whereas those of Group 2 Pls are less than 204 MPa (N=97). The Group 1 data are calculated from the cores of Pl

phenocrysts, whereas Group 2 data are from the rims of Pl phenocrysts and Pl groundmass (see Table S4 for details). This finding is consistent with the crystallization pressure calculated by plagioclase at Site U1347 (Husen et al., 2013; van Gerve et al., 2020) by the eq. 25a of Putirka (2008). Previous studies also showed two distinct pressure groups (I: 727 to 745 MPa, N=125; II: less than 207 MPa, N=2844)(Husen et al., 2013; van Gerve et al., 2020), which are almost the same to ours, suggesting that there are at least two magmatic environments at Tamu Massif.

5.2 Magmatic processes within different magmatic environments revealed by mineral chemistry

Based on the discussion above, we identified two different magmatic environments (Figs. 10 and S5): Environment A is located within the lower crust (~ 25 km depth with magma temperature over 1220 ℃; assuming an average crustal density of 2980 kg/m^3 following Zhang et al. (2016)) and Environment B is located within the upper crust (~ 7 km depth with magma temperature ~ 1140 ℃). As shown in Figs. 4e-4h, the cores of Pl phenocrysts (An > 85) with high crystallization pressure (> 700 MPa) are crystallized in the Environment A, whereas the rims (An < 80) with low crystallization pressure (< 204 MPa) are crystallized in the Environment B. Many Pl phenocrysts show normal zoning (Figs. 3b and 4e), suggesting the progressively evolving composition of the melt during the solidification processes in a closed system (Ginibre et al., 2007; Streck, 2008). Previous study has shown that magmatic recharge was frequent and produced various dissolution textures in plagioclase from Site U1347

353 at Tamu Massif (van Gerve et al., 2020). Moreover, groundmass plagioclase from Site
354 U1347 had skeletal growth habits, indicative of growth at high degrees of undercooling
355 (> 40 °C). However, in this study, Pl phenocrysts at Site 1213 do not have oscillatory
356 textures or cellular textures (Fig. 3), which could be attributed to magma recharge or
357 mixing. In thin sections, we do not find obvious skeletal growth features in either the
358 rims of plagioclase phenocrysts or in groundmass (Fig. 3), which suggests relatively
359 low cooling rates, and our finding is consistent with the previous study at Site 1213
360 (Koppers et al., 2010). According to the low crystallization pressure of the rims of Pl
361 phenocrysts (< 204 MPa; Fig. 4h), they probably formed in the Environment B and
362 during the final ascent from Environment B to the surface. They crystallized in
363 equilibrium with the final erupted liquids, but the cores of Pl phenocrysts crystallized
364 from a more primitive melt. Consequently, we propose that the zoning patterns of Pl
365 phenocryst are attributed to the magma differentiation across a range of pressure and
366 temperature conditions in a closed system. Unlike plagioclase, however, Cpx crystals
367 show a continuous and wide range of crystallization temperature and pressure (Fig. 10),
368 indicating that they may crystallize during ascent from Environment A to B.

369 van Gerve, T.D. et al (2020) used lava samples drilled from Site 1347A at Tamu
370 Massif and concluded that the three environments represent three vertically distinct
371 crystal storage regions (A: 800 MPa; B: 500 MPa; C: 70±120 MPa). However, in this
372 study we do not recognize the storage region with crystallization pressure of 500 MPa.
373 Actually, the exact storage pressures of magmatic environments located within the
374 lower crust (⩾500 MPa) should be interpreted with caution because the pressures from

van Gerve, T.D. et al (2020) were derived from models by using the Haleyjabunga-type lava composition from Iceland (Neave et al., 2019), which might not be perfectly representative of the true melts at Tamu Massif. Despite this fact, another reasonable explanation is that Tamu Massif might have different storage region distributions at different ocean drilling coring sites, suggesting a complex magmatic system beneath Tamu Massif. However, more work are required to confirm this in the future. Regarding the shallow magmatic environment, our results are in agreement with the previous studies using plagioclase (van Gerve et al., 2020) and volcanic glass (Husen et al., 2013; Husen et al., 2016). In summary, we consider that two different magmatic environments are reasonable for us to illuminate the magma plumbing system processes of Tamu Massif.

Deciphering the crystal fractionation history within different magmatic environments is critical for us to investigate magma plumbing system (Kahl et al., 2015; Lee and Bachmann, 2014). By using chemical composition of erupting lava, we can constrain the crystal fractionation history and the composition of primary magma (Herzberg and Asimow, 2008; Lee et al., 2009; Yang and Zhou, 2013). In recent years, many attempts have already been made at Shatsky Rise (Husen et al., 2013; Husen et al., 2016; Sano et al., 2012). Compared with whole-rock geochemistry, in-situ composition of minerals can also shed light on the crystal fractionation history within different magmatic environments.

In this study, the slightly positive correlation between Al_2O_3 and CaO versus $Mg\#_{Cpx}$ values and the strong negative correlation between FeO and Na_2O versus

397 $Mg\#_{Cpx}$ values suggest fractionation of Pl and Cpx (Fig. 6). When $Mg\#_{Cpx}$ values ≤
398 ~80, interestingly, the correlation between Na_2O, Al_2O_3 and CaO contents versus
399 $Mg\#_{Cpx}$ separates into two trend lines. The Cpxs that plot on the green trend line
400 (hereafter defined as Type 1) have higher Na_2O, Al_2O_3 and CaO contents than those of
401 the Cpxs plotted on the grey trend line (hereafter defined as Type 2), suggesting that
402 these Cpxs may have different crystallization history. The relatively low Na_2O, Al_2O_3
403 and CaO contents suggest that Type 2 Cpxs probably crystallized after significant
404 amounts of plagioclase had already been crystallized from the melt or the crystallization
405 pressure of Type 2 Cpxs is relatively lower than Type 1 Cpxs (Neave and Maclennan,
406 2020).

407 To further elucidate the destiny of crystals along the evolutionary path of lavas,
408 we need firstly to constrain the fractional crystallization sequence (Molendijk et al.,
409 2022; Valer et al., 2017; Wang et al., 2021). According to the high-pressure
410 crystallization experiments from synthetic analogues of naturally quenched basaltic
411 glasses recovered at Shatsky Rise (Husen et al., 2016), we find that at high pressure
412 (700 MPa) or under low-H_2O conditions (~0.4 wt.% H_2O), the sequence of crystal
413 fractionation is Ol-Cpx-Pl. The geological setting of Shatsky Rise matches well with
414 the above two conditions: the thickened oceanic crust of Tamus Massif provides high
415 crystallization pressure (Korenaga and Sager, 2012; Zhang et al., 2016). Compared with
416 normal MORB (N-MORB), basalts from oceanic plateau (e.g. Kerguelen, Ontong Java,
417 and Shatsky Rise) are typically abyssal tholeiites with lower H_2O contents (Husen et
418 al., 2013; Husen et al., 2016; Roberge et al., 2004; Sano et al., 2012; Shimizu et al.,

2013; Wallace, 2002). Therefore, it is most likely that Cpx is one of the dominant fractionating phases at the early stage of magma evolution (e.g., Environment A in this study) and Pl did not become a dominant fractionating phase until $Mg\#_{Cpx}$ value is lower than ~80 (Fig.6). In this study, we define the dominant fractionating phase as the most massive mineral phase during the crystallization processes or could make notable influence on the liquid line of descent. When the ascending magma transports to the shallow magmatic environment B, the Pl gradually replaced Cpx as the dominant fractionating phase. When $Mg\#_{Cpx}$ value is lower than ~ 70, the hypothetical melts in equilibrium with groundmass from Site 1213B display negative Eu anomalies (Fig. 7), which also suggests that Pl is the dominated phase at the late stage. Based on the discussion above, we suggest that Type 1 Cpx crystallized at greater depth (e.g., Environment A) and prior to the onset of plagioclase crystallization, whereas Type 2 Cpx crystallized at shallower depth (e.g., Environment B) and after significant plagioclase crystallization. Note that the similarities of Mg# between Type 1 and 2 Cpx suggest that we have similar ranges of melt evolution in both environments, which may indicate different source melt compositions have input in the system.

Clinopyroxene crystals trapped by growing Pl crystals provide distinct records of magmatic evolution to track pre- and syn-eruptive pathways of magma movement towards the surface (Ubide et al., 2021). In Fig. S6, Cpxs are present as inclusions in the Pl crystal, which suggests that these Cpxs crystallized earlier than the host Pl. Based on the Mg#, An, and pressure, we propose that the ascending magma crystallized the Cpxs (P = 240 and 244 MPa in Fig. S6) during ascent from Environment A to B. When

441 the magma cooled and decompressed to low pressures within Environment B, the Pl
442 crystal (P = 50 MPa in Fig. S6) crystallized from the residual melt and then the Cpx
443 trapped in the Pl crystal.
444
445 **5.3 A two-stage model for Shatsky Rise confirmed by MELTS modelling**
446 Since errors for geothermobarometer are inevitable (Putirka, 2008; Wieser et al.,
447 2023) and in order to further clarify the magma plumbing system of Shatsky Rise, we
448 also applied MELTS_EXCEL (Gualda and Ghiorso, 2015) to constrain the
449 crystallization history of the study area. As the starting materials, the best sample for
450 MELTS modelling requires primitive magma composition that had only experienced
451 olivine crystallization. These relatively primary rocks should have high MgO content
452 and olivines with high forsterite content (Fo: $100 \times Mg/(Mg+Fe^{2+}) > 90$). However, no
453 such fresh rocks have been recovered from Shatsky Rise (Sager et al., 2016). Thus,
454 previous studies took high-Mg Kroenke type basalts from the Ontong Java Plateau
455 (Husen et al., 2013) and MORB-like Haleyjabunga lavas (MgO > 10 wt.%) from
456 Iceland (van Gerve et al., 2020) as the starting materials to model the liquid line of
457 descent at Shatsky Rise. However, these two samples obviously have no genetic
458 relationship with those of Shatsky Rise and will bring large uncertainty in the modeling
459 results. Therefore, in this study, we use the sample of Site U1349-12R-4 basalts from
460 Ori Massif with the highest value of MgO (12.3 wt.%) (CHEN Jing et al., 2023) to
461 represent the parental magma. The studied samples are also characterized by relatively
462 high Cr (554 ppm) and Ni (269 ppm) contents, suggesting that they may have

463 undergone limited mineral fractional crystallization.

464 We set the starting temperature to be 1370 ℃ which is the T_P of the Shatsky Rise
465 magma based on the numerical trace element mass balance model considering a
466 pyroxenite-bearing peridotite source mantle (Kimura and Kawabata, 2015) and under
467 the quartz-fayalite-magnetite (QFM) buffer (Carmichael and Ghiorso, 1986). The
468 modeling was carried out at pressures of 400 MPa and 300 MPa, and the temperature
469 ranged from 1370 °C to 1130 °C in steps of 5 °C. For each pressure, we modeled three
470 sets of experiments with different water contents of basalt melts. The water contents
471 were set to be 0 wt.%, 0.1 wt.% and 0.2 wt.% after normalization to unity, based on the
472 estimates of water contents from previous studies (Husen et al., 2013; Husen et al.,
473 2016; Shimizu et al., 2013). As shown in Fig. 11, most of the glass data from previous
474 studies (Table S3) are consistent with the MELTS modeling results. The detailed
475 modeling processes and compositions of the residual melt are shown in Table S5.

476 For all the runs, the olivine was the first phase to crystallize (Fig. S7). The trends
477 of the liquid line of descent for Al_2O_3, TiO_2, Na_2O and K_2O change dramatically at MgO
478 = ~9.6 wt.% (Fig. 11). When MgO values ⩾ ~9.6 wt.%, the slightly increasing TiO_2
479 and FeO_T (not shown) contents and significantly increasing Al_2O_3 contents with
480 decreasing MgO indicate crystallization of olivine and clinopyroxene rather than
481 plagioclase (van Gerve et al., 2020). When MgO values ⩽ ~ 9.6 wt.%, the positive
482 correlation between Al_2O_3 and MgO contents and significantly increasing TiO_2 contents
483 with decreasing MgO (Figs. 11a and 11c) suggest fractional crystallization of
484 plagioclase (Chen et al., 2021). The increasing Na_2O and K_2O contents with decreasing

MgO suggest the fractional crystallization of olivine and clinopyroxene is still significant (Figs. 11b and 11d). In other mafic magmatic systems with thickened oceanic crust (e.g., Iceland), previous study has also suggested that clinopyroxene replaced plagioclase as the third liquidus phase at the early stage of magma evolution (Mutch et al., 2019) and the phenomenon observed experimentally at pressures greater than 600 MPa (Bender et al., 1978; Scott Weaver and Langmuir, 1990). With the increasing water contents and the crystallization pressure, the Al_2O_3 increased and TiO_2 contents decreased, indicating that anhydrous and low-pressure conditions seem to favor the crystallization of more plagioclase (Fig. 11). With the increasing water contents, the cotectic proportion of Pl surpasses this of Cpx at lower temperatures (Fig.S7), also suggesting anhydrous conditions seem to favor the crystallization of more plagioclase. Furthermore, MELTS modeling offers the opportunity to not only track melt compositions, but also the compositions of the minerals being formed (Gualda et al., 2012). We compare the MELTS-derived Cpx compositions with our measured ones (Fig. S8) and find most of the measured Cpxs are consistent with the MELTS modeling results. In conclusion, we suggest that Cpx is one of the dominant fractionating phases at magmatic environment A and Pl gradually replaced Cpx as the dominant fractionating phase at the shallow magmatic environment B.

Based on the discussion above, most of Cpxs from Tamu Massif should record deep crystallization depth, however, we find fewer Cpxs that record deep crystallization depth (>17 km) relative to Pls (Fig.5). These may be due to the errors for geothermobarometer, or most of Cpxs which crystallized over 17 km are just not

recovered. Based on the crystal density from MELTS modeling, the clinopyroxene with relatively high density (3.22 g/cm^3) compared with plagioclase (2.69 g/cm^3) may be accumulated in the deep crust. The plagioclase that crystallized from Environment A have relatively low density and could float on the top of ascending magma (Lange et al., 2013), resulting in recovering them at the Tamu Massif. Our findings are supported by the recent studies of Husen et al. (2016) and van Gerve et al. (2020) in the area. Based on our new results above, we present a two-stage petrologic model to reveal the evolutionary path of lavas and magma plumbing system processes at Tamu Massif (Fig. 12).

5.4 Diffusion timescales and ascent rate at Tamu Massif and the implication

Diffusion modeling of Mg in compositionally zoned plagioclase phenocrysts was carried out to calculate diffusion timescales at Tamu Massif. The diffusion of Mg was modelled using the method of Fabbro et al. (2017) and Costa et al. (2003), the diffusion coefficient of Van Orman et al. (2014), and the partition coefficients of Mutch et al. (2022). One-dimensional models were run as a single step at 1140 °C assuming that the Mg contents of the overgrowths were initially the same as those of the rims. Further details of the modelling are included in Supplementary Text S3.

In this study, out of seven potential plagioclase crystals (Fig. S9), only 3 showed sufficient compositional zoning to allow for diffusion modelling (Fig. 13). Our model assumes that diffusion started only after the entire crystal had grown and calculates the average residence time for the crystal (Costa et al., 2003; Druitt et al., 2012).

Equilibrium profiles were calculated assuming that the outermost analysis was in equilibrium with the melt, then working inward assuming that each successive analysis was in equilibrium with the analysis before. For the diffusion modelling crystals (Fig. 13), we assumed that the high-An rims (An > 70) were in equilibrium with the cores, and the low-An rims (An < 70) initially had the same Mg content as the high-An rims. Thus, by assuming a step function, we can constrain the maximum time that the rims could have survived at high temperature (Costa et al., 2003).

Element diffusion is likely to have been associated with the cooling of the resident melt in Environment B following disaggregation of slightly cooler mushes from the chamber margins (Mutch et al., 2019) or during the final ascent from Environment B to the surface. The best-fitting models yield maximum residence times of 6.27 ~ 93.9 hours at 1140 °C (Fig. 13) and according to our analysis, the shorter timescales (6.27 h) is more likely to represent the final transport time from the shallow magmatic environment B to eruption on the seafloor. Combined with the depth estimates from geobarometry (approximately 2~7 km for Environment B), the calculated pre-eruptive magma ascent rates of Tamu Massif range from ~0.08 to 0.31 m/s (Fig. 14). It should be noted that the magma ascent rates of Tamu Massif are indistinguishable with the ascent rates of fast spreading ridge systems (Chavrit et al., 2012; Gardner et al., 2016; Soule et al., 2012), but faster than those of southwest Indian ridge (Ma et al., 2024). Mutch, E., et al. (2019) combined diffusion modelling timescales with the depth estimates from geobarometry to obtain Moho-to-surface transport rates of 0.02 to 0.1 m/s in Iceland, which seems to be slower than Tamu Massif.

Although the methods for obtaining magma ascent rates are different, for comparison, magma ascent rate of Tamu Massif is about an order of magnitude slower than those estimated for volatile-rich magmas in explosive arc volcanos (Lloyd et al., 2014). Furthermore, magma ascent rates of ocean island settings (such as Hawaii(Peslier et al., 2015) and kimberlites (Peslier et al., 2008) with more enriched magma suites and deeper depth of origin were much faster than those estimated for Tamu Massif, indicating that enriched magma suites and volatiles play the importance roles in controlling magma dynamics. Geophysical data from Tamu Massif demonstrated that large volumes of material rose from the mantle to the lithosphere in short periods of time to build this great volcanic edifice (Sager et al., 2013), suggesting a relatively high magma production rate at Tamu Massif. Thus, we propose that the relatively high magma production rate, which controls magma chamber overpressure (Cassidy et al., 2018), does not produce a high magma ascent rate to some extent, at least at Tamu Massif. One reasonable explanation is that the mantle-derived magmas at Tamu Massif would not travel from their upper mantle sources to erupt at the Earth's surface directly like oceanic intraplate explosive eruptions (DeVitre et al., 2023) and kimberlites (Casetta et al., 2023; Peslier et al., 2008), on the contrary they would stagnate within the deep magmatic environment (i.e., Environment A in Fig. 12) exceeded several thousand years (van Gerve et al., 2020). Altogether, our study provides constraints on crystal storage timescales within the shallow Environment B ranging from a few hours to a few days and a magma ascent rate of ~0.08 to 0.31 m/s at Tamu Massif (Fig. 14).

6. Conclusions

In this study, we present the major and trace element data for clinopyroxene and plagioclase at Site 1213 to elucidate the magmatic ascent processes of Tamu Massif. Combined with modeling and previous studies, our results lead to the following conclusions:

(1) Based on the mineral chemistry and P-T calculations, we can identify two types of Cpx and two groups of Pl. Type 1 Cpxs with higher Al_2O_3 (~3 wt.%), CaO (17~19 wt.%) and Na_2O (0.3~0.4 wt.%) crystallized at greater depth and prior to the onset of plagioclase crystallization, whereas Type 2 Cpxs with relatively lower Al_2O_3 (~1.5 wt.%), CaO (14~16 wt.%) and Na_2O (0.2~0.3 wt.%) crystallized at shallower depth and after significant plagioclase crystallization. The Pl can be divided into two groups: Group 1 are from the core of the Pl phenocrysts with high crystallization pressure (727 to 733 MPa) and An value (~ 85), whereas Group 2 are from the rim of the Pl phenocrysts and Pl groundmass with low crystallization pressure (< 204 MPa) and An value (< 75).

(2) According to the MELTS modeling, we propose that the sequence of crystal fractionation is Ol-Cpx-Pl at Tamu Massif and suggest Pl gradually replaced Cpx as the dominant fractionating phase at the shallow magmatic environment B. The magma ascent rates of Tamu Massif are indistinguishable with the ascent rates of fast spreading ridge systems, but slower than those of volatile-rich magmas in arc volcanoes and kimberlites.

(3) Combined with mineral chemistry and modeling, we propose a two-stage petrologic model to reveal the evolutionary path of lavas and magma plumbing system processes at Tamu Massif. Environment A is located within the lower crust (~ 25 km depth) with high crystal crystallization temperature (> 1220 ℃) and Environment B is located within the upper crust (~ 7 km depth) with low crystal crystallization temperature (~ 1140 ℃). The final transport time from Environment B to eruption on the seafloor is usually within a few days (6.27–93.9 hours). Overall, this study helps us improve our understanding of the formation and evolution of other oceanic plateaus associated with thickened oceanic crust around the world.

Declaration of Competing Interest

We have no known competing financial interests or personal relationships that could have appeared to influence the work reported in this paper.

Acknowledgments

We are very grateful to Penny Wieser and Matthew Gleeson for answering a lot of questions about the Thermobar and PetThermoTools, as well as very helpful discussions regarding diffusion chronometry. We thank Jordan Lubbers for helping with diffusion chronometry and developing open-source Python tools, and Morgan Williams for his pyrolite tool and helpful advice. Martin Mangler, Alice MacDonald and editor Jane H. Scarrow are thanked for their constructive comments that led to improvements on this manuscript. This research used samples provided by the Ocean Drilling Program

(ODP). This study was supported by the National Key Research and Development Program of China (2023YFF0803404), the Project of Sanya Yazhou Bay Science and Technology City, Grant No: SCKJ-JYRC-2023-56 and the National Natural Science Foundation of China (Nos. 42072069).

References:

Aigner-Torres, M., Blundy, J., Ulmer, P. and Pettke, T., 2007. Laser Ablation ICPMS study of trace element partitioning between plagioclase and basaltic melts: an experimental approach. Contributions to Mineralogy and Petrology, 153(6): 647-667.

Baxter, R.J.M., Maclennan, J., Neave, D.A. and Thordarson, T., 2023. Depth of Magma Storage Under Iceland Controlled by Magma Fluxes. Geochemistry, Geophysics, Geosystems, 24(7).

Bender, J.F., Hodges, F.N. and Bence, A.E., 1978. Petrogenesis of basalts from the project FAMOUS area: experimental study from 0 to 15 kbars. Earth and Planetary Science Letters, 41(3): 277-302.

Bennett, E.N., Lissenberg, C.J. and Cashman, K.V., 2019. The significance of plagioclase textures in mid-ocean ridge basalt (Gakkel Ridge, Arctic Ocean). Contributions to Mineralogy and Petrology, 174(6).

Bergman, S.C., Eldrett, J.S. and Minisini, D., 2021. Phanerozoic Large Igneous Province, Petroleum System, and Source Rock Links. Geophysical Monograph Series, pp. 191-228.

Black, B.A., Karlstrom, L. and Mather, T.A., 2021. The life cycle of large igneous provinces. Nature Reviews Earth & Environment, 2(12): 840-857.

Bralower, T.J., Premoli Silva, I. and Malone, M.J., 2002. Proceedings of the Ocean Drilling Program, Initial Reports Volume 198.

Bryan, S.E. and Ernst, R.E., 2008. Revised definition of Large Igneous Provinces (LIPs). Earth-Science Reviews, 86(1-4): 175-202.

Buchan, K.L. and Ernst, R.E., 2021. Plumbing systems of large igneous provinces (LIPs) on Earth and Venus: Investigating the role of giant circumferential and radiating dyke swarms, coronae and novae, and mid-crustal intrusive complexes. Gondwana Research, 100: 25-43.

Campbell, I.H., 2005. Large Igneous Provinces and the Mantle Plume Hypothesis. Elements, 1(5): 265-269.

Caracciolo, A. et al., 2023. Magma plumbing architectures and timescales of magmatic processes during historical magmatism on the Reykjanes Peninsula, Iceland. Earth and Planetary Science Letters, 621: 118378.

Carlson, R.W., Lugmair, G.W. and Macdougall, J.D., 1981. Crustal influence in the generation of continental flood basalts. Nature, 289(5794): 160-162.

Carmichael, I.S.E. and Ghiorso, M.S., 1986. Oxidation-reduction relations in basic magma: a case for homogeneous equilibria. Earth and Planetary Science Letters, 78(2): 200-210.

Casetta, F. et al., 2023. Ascent rate of the Udachnaya-East kimberlite melts from olivine diffusion chronometry. Earth and Planetary Science Letters, 619: 118322.

Cassidy, M., Manga, M., Cashman, K. and Bachmann, O., 2018. Controls on explosive-effusive volcanic

eruption styles. Nat Commun, 9(1): 2839.
Chavrit, D., Humler, E., Morizet, Y. and Laporte, D., 2012. Influence of magma ascent rate on carbon dioxide degassing at oceanic ridges: Message in a bubble. Earth and Planetary Science Letters, 357-358: 376-385.
CHEN Jing, CHEN ShuangShuan, GAO Rui and LIU JiaQi, 2023. Geochemical characteristics of Shatsky Rise Cretaceous basalts and implication on the interaction between mantle plume and mid-ocean ridge. Acta Petrologica Sinica, 39(8): 2379-2401.
Chen, S. et al., 2021. Coexistence of Hainan Plume and Stagnant Slab in the Mantle Transition Zone beneath the South China Sea Spreading Ridge: Constraints from Volcanic Glasses and Seismic Tomography. Lithosphere, 2021(Special 2): 6619463.
Chen, S., Liu, J., Gao, R. and Wang, Z., 2021. Geochemistry of Cretaceous basalts from the Ontong Java Plateau: Implications for the off-axis plume–ridge interaction. Chemical Geology, 564: 119815.
Coffin, M.F. and Eldholm, O., 1992. Volcanism and continental break-up: a global compilation of large igneous provinces. Geological Society, London, Special Publications, 68(1): 17-30.
Coffin, M.F. and Eldholm, O., 1994. Large igneous provinces: Crustal structure, dimensions, and external consequences. Reviews of Geophysics, 32(1): 1-36.
Costa, F., Chakraborty, S. and Dohmen, R., 2003. Diffusion coupling between trace and major elements and a model for calculation of magma residence times using plagioclase. Geochimica et Cosmochimica Acta, 67(12): 2189-2200.
Costa, F., Shea, T. and Ubide, T., 2020. Diffusion chronometry and the timescales of magmatic processes. Nature Reviews Earth & Environment, 1(4): 201-214.
Courtillot, V.E. and Renne, P.R., 2003. On the ages of flood basalt events. Comptes Rendus Geoscience, 335(1): 113-140.
DeVitre, C.L. et al., 2023. Oceanic intraplate explosive eruptions fed directly from the mantle. Proceedings of the National Academy of Sciences, 120(33).
Druitt, T.H., Costa, F., Deloule, E., Dungan, M. and Scaillet, B., 2012. Decadal to monthly timescales of magma transfer and reservoir growth at a caldera volcano. Nature, 482(7383): 77-80.
Ernst, R.E. et al., 2021. Large Igneous Province Record Through Time and Implications for Secular Environmental Changes and Geological Time-Scale Boundaries. Geophysical Monograph Series, pp. 1-26.
Ernst, R.E. and Jowitt, S.M., 2013. Large Igneous Provinces (LIPs) and Metallogeny. In: M. Colpron, T. Bissig, B.G. Rusk and J.F.H. Thompson (M. Colpron, T. Bissig, B.G. Rusk and J.F.H. Thompson(Editors), Tectonics, Metallogeny, and Discovery: The North American Cordillera and Similar Accretionary Settings. Society of Economic Geologists, pp. 0.
Ernst, R.E., Liikane, D.A., Jowitt, S.M., Buchan, K.L. and Blanchard, J.A., 2019. A new plumbing system framework for mantle plume-related continental Large Igneous Provinces and their mafic-ultramafic intrusions. Journal of Volcanology and Geothermal Research, 384: 75-84.
Gardner, J.E., Jackson, B.A., Gonnermann, H. and Soule, S.A., 2016. Rapid ascent and emplacement of basaltic lava during the 2005–06 eruption of the East Pacific Rise at ca. 9°51′ N as inferred from CO2 contents. Earth and Planetary Science Letters, 453: 152-160.
Ginibre, C., Wo¨rner, G. and Kronz, A., 2007. Crystal Zoning as an Archive for Magma Evolution. Elements, 3(4): 261-266.
Gualda, G.A.R. and Ghiorso, M.S., 2015. MELTS_Excel: A Microsoft Excel-based MELTS interface for research and teaching of magma properties and evolution. Geochemistry, Geophysics, Geosystems,

16(1): 315-324.
Gualda, G.A.R., Ghiorso, M.S., Lemons, R.V. and Carley, T.L., 2012. Rhyolite-MELTS: a Modified Calibration of MELTS Optimized for Silica-rich, Fluid-bearing Magmatic Systems. Journal of Petrology, 53(5): 875-890.
Harper, M. et al., 2015. python-ternary: Ternary Plots in Python. Zenodo.
Hellevang, B. and Pedersen, R.B., 2008. Magma Ascent and Crustal Accretion at Ultraslow-Spreading Ridges: Constraints from Plagioclase Ultraphyric Basalts from the Arctic Mid-Ocean Ridge. Journal of Petrology, 49(2): 267-294.
Herzberg, C. and Asimow, P.D., 2008. Petrology of some oceanic island basalts: PRIMELT2.XLS software for primary magma calculation. Geochemistry, Geophysics, Geosystems, 9(9).
Heydolph, K. et al., 2014. Plume versus plate origin for the Shatsky Rise oceanic plateau (NW Pacific): Insights from Nd, Pb and Hf isotopes. Lithos, 200-201: 49-63.
Holness, M.B. et al., 2007. Textures in Partially Solidified Crystalline Nodules: a Window into the Pore Structure of Slowly Cooled Mafic Intrusions. Journal of Petrology, 48(7): 1243-1264.
Hooper, P.R., 1990. The timing of crustal extension and the eruption of continental flood basalts. Nature, 345(6272): 246-249.
Huang, Y. et al., 2018. Magnetic anomaly map of Ori Massif and its implications for oceanic plateau formation. Earth and Planetary Science Letters, 501: 46-55.
Husen, A. et al., 2013. Geothermobarometry of basaltic glasses from the Tamu Massif, Shatsky Rise oceanic plateau. Geochemistry, Geophysics, Geosystems, 14(10): 3908-3928.
Husen, A., Almeev, R.R. and Holtz, F., 2016. The effect of H2O and pressure on multiple saturation and liquid lines of descent in basalt from the Shatsky Rise. Journal of Petrology, 57(2): 309–344.
Jiang, Q., Jourdan, F., Olierook, H.K.H. and Merle, R.E., 2023. An appraisal of the ages of Phanerozoic large igneous provinces. Earth-Science Reviews, 237: 104314.
Kahl, M., Chakraborty, S., Pompilio, M. and Costa, F., 2015. Constraints on the nature and evolution of the magma plumbing system of Mt. Etna Volcano (1991-2008) from a combined thermodynamic and kinetic modelling of the compositional record of minerals. Journal of petrology, 56(10): 2025-2068.
Kimura, J. and Kawabata, H., 2015. Ocean Basalt Simulator version 1 (OBS1): Trace element mass balance in adiabatic melting of a pyroxenite-bearing peridotite. Geochemistry, Geophysics, Geosystems, 16(1): 267-300.
Kinman, W.S. and Neal, C.R., 2006. Magma evolution revealed by anorthite-rich plagioclase cumulate xenoliths from the Ontong Java Plateau: Insights into LIP magma dynamics and melt evolution. Journal of Volcanology and Geothermal Research, 154(1-2): 131-157.
Koppers, A.A.P. et al., 2010. Massive basalt flows on the southern flank of Tamu Massif, Shatsky Rise: a reappraisal of ODP Site 1213 basement units, 324. Integrated Ocean Drilling Program Management International, Inc., Tokyo.
Korenaga, J. and Sager, W.W., 2012. Seismic tomography of Shatsky Rise by adaptive importance sampling. Journal of Geophysical Research: Solid Earth, 117.
Lange, A.E., Nielsen, R.L., Tepley III, F.J. and Kent, A.J.R., 2013. The petrogenesis of plagioclase-phyric basalts at mid-ocean ridges. Geochemistry, Geophysics, Geosystems, 14(8): 3282-3296.
Lee, C.A. and Bachmann, O., 2014. How important is the role of crystal fractionation in making intermediate magmas? Insights from Zr and P systematics. Earth and Planetary Science Letters, 393: 266-274.
Lee, C.A., Luffi, P., Plank, T., Dalton, H. and Leeman, W.P., 2009. Constraints on the depths and

temperatures of basaltic magma generation on Earth and other terrestrial planets using new thermobarometers for mafic magmas. Earth and Planetary Science Letters, 279(1-2): 20-33.
Li, S. et al., 2016. Orientation of joints and arrangement of solid inclusions in fibrous veins in the Shatsky Rise, NW Pacific: implications for crack-seal mechanisms and stress fields. Geological Journal, 51: 562-578.
Li, X. et al., 2020. Integrated major and trace element study of clinopyroxene in basic, intermediate and acidic volcanic rocks from the middle Okinawa Trough: Insights into petrogenesis and the influence of subduction component. Lithos, 352-353: 105320.
Liu, Y. et al., 2008. In situ analysis of major and trace elements of anhydrous minerals by LA-ICP-MS without applying an internal standard. Chemical Geology, 257(1-2): 34-43.
Lloyd, A.S. et al., 2014. NanoSIMS results from olivine-hosted melt embayments: Magma ascent rate during explosive basaltic eruptions. Journal of Volcanology and Geothermal Research, 283: 1-18.
Ma, B. et al., 2024. Trans-Lithospheric Ascent Processes of the Deep-Rooted Magma Plumbing System Underneath the Ultraslow-Spreading SW Indian Ridge. Journal of Geophysical Research: Solid Earth, 129(1): e2023JB027224.
Mahoney, J., Duncan, R., Tejada, M.L., Sager, W. and Bralower, T., 2005. Jurassic-Cretaceous boundary age and mid-ocean-ridge type mantle source for Shatsky Rise. Geology, 33: 185.
Métrich, N. et al., 2014. Is the ‘Azores Hotspot’ a Wetspot? Insights from the Geochemistry of Fluid and Melt Inclusions in Olivine of Pico Basalts. Journal of Petrology, 55(2): 377-393.
Mittal, T., Richards, M.A. and Fendley, I.M., 2021. The Magmatic Architecture of Continental Flood Basalts I: Observations From the Deccan Traps. Journal of Geophysical Research: Solid Earth, 126(12): e2021JB021808.
Molendijk, S.M., Buchs, D.M., Mason, P.R.D. and Blundy, J.D., 2022. Clinopyroxene diversity and magma plumbing system processes in an accreted Pacific ocean island, Panama. Contributions to Mineralogy and Petrology, 177(2): 30.
Mutch, E.J.F., Maclennan, J., Holland, T.J.B. and Buisman, I., 2019. Millennial storage of near-Moho magma. Science, 365(6450): 260-264.
Mutch, E.J.F., Maclennan, J., Shorttle, O., Edmonds, M. and Rudge, J.F., 2019. Rapid transcrustal magma movement under Iceland. Nature Geoscience, 12(7): 569-574.
Nakanishi, M., Sager, W.W. and Klaus, A., 1999. Magnetic lineations within Shatsky Rise, northwest Pacific Ocean: Implications for hot spot-triple junction interaction and oceanic plateau formation. Journal of Geophysical Research: Solid Earth, 104(B4): 7539-7556.
Nakanishi, M., Sager, W.W. and Korenaga, J., 2015. Reorganization of the Pacific-Izanagi-Farallon triple junction in the Late Jurassic: Tectonic events before the formation of the Shatsky Rise. In: C.R. Neal, W.W. Sager, T. Sano and E. Erba (C.R. Neal, W.W. Sager, T. Sano and E. Erba)^(C.R. Neal, W.W. Sager, T. Sano and E. Erbas)|,*. Geological Society of America, pp. 0.
Neal, C.R., Coffin, M.F. and Sager, W.W., 2019. Contributions of scientific ocean drilling to understanding the emplacement of submarine large igneous provinces and their effects on the environment. Oceanography, 32(1): 176–192.
Neave, D.A. and Maclennan, J., 2020. Clinopyroxene Dissolution Records Rapid Magma Ascent. Frontiers in Earth Science, 8.
Neave, D.A. and Putirka, K.D., 2017. A new clinopyroxene-liquid barometer, and implications for magma storage pressures under Icelandic rift zones. American Mineralogist, 102(4): 777-794.
Neave, D.A., Namur, O., Shorttle, O. and Holtz, F., 2019. Magmatic evolution biases basaltic records of

mantle chemistry towards melts from recycled sources. Earth and Planetary Science Letters, 520: 199-211.
Neave, D.A., Passmore, E., Maclennan, J., Fitton, G. and Thordarson, T., 2013. Crystal – Melt Relationships and the Record of Deep Mixing and Crystallization in the ad 1783 Laki Eruption, Iceland. Journal of Petrology, 54(8): 1661-1690.
Nixon, A.L. et al., 2022. Low-temperature thermal history of the McArthur Basin: Influence of the Cambrian Kalkarindji Large Igneous Province on hydrocarbon maturation. Basin Research, 34(6): 1936-1959.
Peace, A.L. et al., 2020. A review of Pangaea dispersal and Large Igneous Provinces – In search of a causative mechanism. Earth-Science Reviews, 206: 102902.
Peslier, A.H., Bizimis, M. and Matney, M., 2015. Water disequilibrium in olivines from Hawaiian peridotites: Recent metasomatism, H diffusion and magma ascent rates. Geochimica et Cosmochimica Acta, 154: 98-117.
Peslier, A.H., Woodland, A.B. and Wolff, J.A., 2008. Fast kimberlite ascent rates estimated from hydrogen diffusion profiles in xenolithic mantle olivines from southern Africa. Geochimica et Cosmochimica Acta, 72(11): 2711-2722.
Petrone, C.M. et al., 2022. Magma recharge and mush rejuvenation drive paroxysmal activity at Stromboli volcano. Nature Communications, 13(1).
Putirka, K.D., 2008. Thermometers and Barometers for Volcanic Systems. Reviews in Mineralogy and Geochemistry, 69(1): 61-120.
Richards, M.A., Duncan, R.A. and Courtillot, V.E., 1989. Flood Basalts and Hot-Spot Tracks: Plume Heads and Tails. Science, 246(4926): 103-107.
Roberge, J., White, R.V. and Wallace, P.J., 2004. Volatiles in submarine basaltic glasses from the Ontong Java Plateau (ODP Leg 192): implications for magmatic processes and source region compositions. Geological Society, London, Special Publications, 229(1): 239-257.
Sager, W.W. et al., 2013. An immense shield volcano within the Shatsky Rise oceanic plateau, northwest Pacific Ocean. Nature Geoscience, 6(11): 976-981.
Sager, W.W. et al., 2019. Oceanic plateau formation by seafloor spreading implied by Tamu Massif magnetic anomalies. Nature Geoscience, 12(8): 661-666.
Sager, W.W., Handschumacher, D.W., Hilde, T.W.C. and Bracey, D.R., 1988. Tectonic evolution of the northern Pacific plate and Pacific-Farallon Izanagi triple junction in the Late Jurassic and Early Cretaceous (M21-M10). Tectonophysics, 155(1): 345-364.
Sager, W.W., Kim, J., Klaus, A., Nakanishi, M. and Khankishieva, L.M., 1999. Bathymetry of Shatsky Rise, northwest Pacific Ocean: Implications for ocean plateau development at a triple junction. Journal of Geophysical Research: Solid Earth, 104(B4): 7557-7576.
Sager, W.W., Sano, T. and Geldmacher, J., 2016. Formation and evolution of Shatsky Rise oceanic plateau: Insights from IODP Expedition 324 and recent geophysical cruises. Earth-Science Reviews, 159: 306-336.
Sager, W.W., Sano, T., Geldmacher, J. and Scientists, T.E., 2010. Proceedings of the Integrated Ocean Drilling Program, 324. Integrated Ocean Drilling Program Management International, Inc., Tokyo.
Sano, T. et al., 2012. Variety and origin of magmas on Shatsky Rise, northwest Pacific Ocean. Geochemistry, Geophysics, Geosystems, 13(8): n/a-n/a.
Scott Weaver, J. and Langmuir, C.H., 1990. Calculation of phase equilibrium in mineral-melt systems. Computers & Geosciences, 16(1): 1-19.

Shcherbakov, V.D., Plechov, P.Y., Izbekov, P.E. and Shipman, J.S., 2011. Plagioclase zoning as an indicator of magma processes at Bezymianny Volcano, Kamchatka. Contributions to Mineralogy and Petrology, 162(1): 83-99.
Shimizu, K., Shimizu, N., Sano, T., Matsubara, N. and Sager, W., 2013. Paleo-elevation and subsidence of ~145 Ma Shatsky Rise inferred from CO2 and H2O in fresh volcanic glass. Earth and Planetary Science Letters, 383: 37–44.
Soule, S.A. et al., 2012. CO2 variability in mid-ocean ridge basalts from syn-emplacement degassing: Constraints on eruption dynamics. Earth and Planetary Science Letters, 327-328: 39-49.
Streck, M.J., 2008. Mineral Textures and Zoning as Evidence for Open System Processes. Reviews in Mineralogy and Geochemistry, 69(1): 595-622.
Sun, C. and Liang, Y., 2012. Distribution of REE between clinopyroxene and basaltic melt along a mantle adiabat: effects of major element composition, water, and temperature. Contributions to Mineralogy and Petrology, 163(5): 807-823.
Tapu, A.T., Ubide, T. and Vasconcelos, P.M., 2022. Plumbing System Architecture of Late-Stage Hotspot Volcanoes in Eastern Australia. Journal of Petrology, 63(3).
Tapu, A.T., Ubide, T. and Vasconcelos, P.M., 2023. Increasing complexity in magmatic architecture of volcanoes along a waning hotspot. Nature Geoscience.
Tucker, J.M. et al., 2019. A high carbon content of the Hawaiian mantle from olivine-hosted melt inclusions. Geochimica et Cosmochimica Acta, 254: 156-172.
Ubide, T., Neave, D.A., Petrelli, M. and Longpré, M., 2021. Crystal Archives of Magmatic Processes. Frontiers in Earth Science, 9.
Valer, M., Bachèlery, P. and Schiano, P., 2017. The Petrogenesis of Plagioclase-ultraphyric Basalts from La Réunion Island. Journal of Petrology, 58(4): 675-698.
van Gerve, T.D., Neave, D.A., Almeev, R.R., Holtz, F. and Namur, O., 2020. Zoned Crystal Records of Transcrustal Magma Transport, Storage and Differentiation: Insights from the Shatsky Rise Oceanic Plateau. Journal of Petrology, 61(8).
Vannucci, R., Bottazzi, P., Wulff-Pedersen, E. and Neumann, E.R., 1998. Partitioning of REE, Y, Sr, Zr and Ti between clinopyroxene and silicate melts in the mantle under La Palma (Canary Islands): implications for the nature of the metasomatic agents. Earth and Planetary Science Letters, 158(1): 39-51.
Wallace, P.J., 2002. Volatiles in Submarine Basaltic Glasses from the Northern Kerguelen Plateau (ODP Site 1140): Implications for Source Region Compositions, Magmatic Processes, and Plateau Subsidence. Journal of Petrology, 43(7): 1311-1326.
Wang, X. et al., 2021. Magnesium isotopic fractionation during basalt differentiation as recorded by evolved magmas. Earth and Planetary Science Letters, 565: 116954.
Wei, X., Zhang, Y., Shi, X., Castillo, P.R. and Xu, Y., 2022. Concurrent magma mixing and crystallization processes revealed by clinopyroxene macrocrysts from Lamont guyot lavas in NW Pacific. Lithos, 428-429: 106833.
White, R.S., McKenzie, D. and O'Nions, R.K., 1992. Oceanic crustal thickness from seismic measurements and rare earth element inversions. Journal of Geophysical Research: Solid Earth, 97(B13): 19683-19715.
Wieser, P. et al., 2022. Thermobar: An open-source Python3 tool for thermobarometry and hygrometry. Volcanica, 5(2): 349-384.
Wieser, P.E. et al., 2023. Barometers Behaving Badly I: Assessing the Influence of Analytical and

Experimental Uncertainty on Clinopyroxene Thermobarometry Calculations at Crustal Conditions. Journal of Petrology, 64(2): egac126.
Wignall, P.B., 2001. Large igneous provinces and mass extinctions. Earth-science reviews, 53(1-2): 1-33.
Williams, M. et al., 2020. pyrolite: Python for geochemistry. The Journal of Open Source Software, 5: 2314.
Winpenny, B. and Maclennan, J., 2011. A Partial Record of Mixing of Mantle Melts Preserved in Icelandic Phenocrysts. Journal of Petrology, 52(9): 1791-1812.
Yang, Z. and Zhou, J., 2013. Can we identify source lithology of basalt? Scientific Reports, 3(1).
Zhang, J. and Chen, J., 2017. Geophysical implications for the formation of the Tamu Massif – the Earth's largest single volcano – within the Shatsky Rise in the northwest Pacific Ocean. Science Bulletin, 62(1): 69-80.
Zhang, J., Sager, W.W. and Korenaga, J., 2016. The seismic Moho structure of Shatsky Rise oceanic plateau, northwest Pacific Ocean. Earth and Planetary Science Letters, 441: 143-154.
Zhang, M., O Reilly, S.Y., Wang, K., Hronsky, J. and Griffin, W.L., 2008. Flood basalts and metallogeny: The lithospheric mantle connection. Earth-Science Reviews, 86(1-4): 145-174.
Zhang, X. et al., 2023. Magmatism of Shatsky Rise controlled by plume – ridge interaction. Nature Geoscience.

Figure Captions

Fig. 1 Bathymetric map of Shatsky Rise with location of ODP and IODP drill sites (Nakanishi et al., 1999). Inset shows the current location of Shatsky Rise in the NW Pacific. Figures are modified after Husen et al. (2013) and Heydolph, K (2014).

Fig. 2 Lithology of Site 1213 at Tamu Massif, showing both basal sediment and igneous sections (Koppers, 2010; Sager et al., 2010). Site 1213 is the first hole to penetrate into igneous basement of Shatsky Rise, on the southwest flank of Tamu Massif. Three igneous units (IVa–IVc) are interpreted as massive flows 8–15 m thick. Roman numbers indicate lithologic units, which are described in Koppers (2010) and Sager et al. (2010). The diamond and triangle represent the clinopyroxene and plagioclase in the thin

907 sections for EPMA and LA-ICP-MS in this study. Mbsf, meters below sea-floor.

908

909 Fig. 3 Cross-polarized light images of Tamu Massif volcanic rocks from Site 1213-29R-
910 1(a), Site 1213-31R-2 (b, c, e), Site 1213-33R-4 (d), Site 1213-31R-4 (f). Cpx,
911 clinopyroxene; Pl, plagioclase.

912

913 Fig. 4 Representative BSE images of zoned Cpx and Pl from volcanic rocks at Tamu
914 Massif. (a-d) are from Site 1213B-32R-2 and (e-h) are from Site 1213B-31R-2. The
915 yellow line in (a) and (d) represent the location of the electron microprobe traverses
916 across the zoning. The analysis results at each point are present below and the distance
917 between any two adjacent points is fixed. The blue dashed line in (a) and (e) represent
918 the zoning of Cpx and Pl. Cpx = clinopyroxene, Pl = plagioclase, Mt = magnetite.

919

920 Fig. 5 Compositions of clinopyroxene phenocrysts and groundmass from the basaltic
921 lavas cored at Site U1213, Shatsky Rise oceanic plateau. The data points are individual
922 measurements obtained for each crystal, plotted in the enstatite-ferrosilite-wollastonite
923 (En-Fs-Wo) ternary diagrams (Morimoto et al., 1988). The data of Cpx crystals at Site
924 U1347 are from Husen, A., et al. (2013) and van Gerve, T.D., et al. (2020). This figure
925 is based on the ternary plot python package (Harper et al., 2015; Wieser et al., 2022).

926

927 Fig. 6 Plots of Al_2O_3 (a), CaO (b), Na_2O (c), and FeO_t (d) versus Mg# in clinopyroxene.
928 The green and grey trend lines represent the fractionation history of different types Cpx

929 that experienced different magma plumbing system processes (see text for details).
930 Vertical dashed lines in (a-c) represent the trend lines start to bifurcate significantly
931 when Mg# $_{Cpx}$ value reached ~80. All the data used here were acquired by EPMA. The
932 data of Cpx crystals at Site U1347 are from Husen, A., et al. (2013) and van Gerve,
933 T.D., et al. (2020).
934
935 Fig. 7 Chondrites-normalized REE diagrams and Primitive mantle-normalized trace
936 element abundances diagrams for Cpx in this study. The grey and purple areas in (a)
937 show REE patterns for hypothetical melts in equilibrium with Cpx phenocryst and
938 groundmass, calculated using partition coefficients (K_D(Fe-Mg) $^{Cpx\text{-}melt}$) from Sun and
939 Liang (2012). Whole-rock data is from Mahoney et al. (2005). Chondrite and primitive
940 mantle normalization values are from McDonough and Sun (1995). This figure is based
941 on the REE plot python package (Williams et al., 2020).
942
943 Fig. 8 Compositions of plagioclase phenocrysts and groundmass from the basaltic lavas
944 cored at Site 1213B and U1347 (Husen 2013), Shatsky Rise oceanic plateau. The data
945 points are individual measurements obtained for each crystal, plotted in the anorthite-
946 albite-orthoclase (An-Ab-Or) ternary diagrams. This figure is based on the ternary plot
947 python package (Harper et al., 2015; Wieser et al., 2022).
948
949 Fig. 9 Plots of Al_2O_3 (a), CaO (b), FeO_T (c), La (d), Eu (e), and La/Y (f) versus An (%)
950 in plagioclases. The purple, red and blue areas circled in (a-c) represent the range of

951 different types of plagioclase compositions from Site U1347 at Tamu Massif (van Gerve
952 et al., 2020).
953
954 Fig. 10 Plots of crystallization pressure versus temperature of Cpx phenocryst and
955 groundmass. The red and blue stars represent Environment A and B from Site 1213 at
956 Tamu Massif. The green areas show crystallization pressure of two groups Pl, calculated
957 using the eq. 25a of Putirka (2008). The data of Cpx crystals at Site U1347 are from
958 Husen, A., et al. (2013) and van Gerve, T.D., et al. (2020).
959
960 Fig. 11 The plots of MgO vs. major elements for volcanic rocks from the Shatsky Rise.
961 The data of Shatsky Rise glass samples are cited from Sano, T., et al. (2012), Shimizu,
962 K., et al. (2013), Husen, A., et al. (2013) and van Gerve, T.D., et al. (2020). The different
963 colored lines are the models calculated by MELTS with different starting H_2O contents.
964 The dashed and solid lines in these diagrams are the modeled differentiation trends with
965 different crystallization pressure. Note that the purple star represents the modelled
966 composition of U1349-12R-4 basalts (CHEN Jing et al., 2023).
967
968 Fig. 12 A two-stage model for the magma plumbing system of Tamu Massif according
969 to in situ major-trace elements of clinopyroxene (Cpx) and plagioclase (Pl) from Site
970 1213 in this study. Environment A is located within the lower crust (~ 25 km depth)
971 with high crystal crystallization temperature (> 1220 °C) and Environment B is located
972 within the upper crust (~ 7 km depth) with low crystal crystallization temperature (~

1140 ℃). Environment B magma is fed by the deeper reservoir Environment A. The OBS reflection Moho is according to Korenaga, J. and W.W. Sager (2012).

Fig. 13 Representative diagrams showing the zoning of plagioclase crystals and corresponding diffusion timescales. The rim-to-core compositional profile is drawn on the plagioclase microscope images (red line). Dashed lines represent the initial compositional distribution profile and green lines represent the best modelling fit Mg profile matching the measured Mg profile.

Fig. 14 Magma ascent rates and literature comparison with other magma in different tectonic settings. The different colors of the ascent rate represent different research methods. The blue represents the numerical modeling of Fe-Mg, Ni, and Mn elements in olivine and plagioclase, the red represents vesicle size distribution and volatile measurements (CO_2 and H_2O), the green is decompression experiment and CO_2 modeling, the purple represents modeling of diffusion-controlled bubble growth, the brown represents modeling the dissolution of clinopyroxene crystals, and the orange represents the modeling of diffusive volatile loss. Figure is modified after Ma, B., et al. (2024).